EUROPEAN ORGANIZATION FOR NUCLEAR RESEARCH

SICAL - a high precision silicon-tungsten luminosity calorimeter for ALEPH

D. Bédérède, E. Beuville, B. Bloch-Devaux, L. Gosset, A. Joudon, E. Lançon, J. Pascual,
J. Perlas[1], B. Peyaud, J. Rander, J.F. Renardy, J.P. Schuller, B. Vallage
Service de Physique des Particules, DAPNIA, CE-Saclay, 91191 Gif-sur-Yvette Cedex, France[2]

R. Benetta, J. Boudreau[3], J. Griffiths, R. Grabit, P. Jarron, B. Lofstedt,
R. Miquel, J.C. Santiard, G. Stefanini, H. Wahl
European Laboratory for Particle Physics (CERN), 1211 Geneva 23, Switzerland

C. Avanzini, C. Cerri, R. Fantechi, R. Lorenzini[4], E.B. Martin[5], G. Pierazzini, A. Valassi
*Dipartimento di Fisica dell'Università, INFN Sezione di Pisa, e Scuola Normale Superiore.
56010 Pisa, Italy*

Abstract

The design, construction and performance of a silicon-tungsten electromagnetic calorimeter built to achieve an experimental luminosity measurement precision at LEP ≤ 0.1 % is described. The detector uses homogeneous construction to give full azimuthal acceptance for Bhabha scattering over polar angles from 24 to 58 mrad. Detailed information concerning shower developement is obtained from zero-suppressed readout of the 12288 pads of the detector. Trigger decisions are generated from a rapid flash-ADC system using programmable gate arrays.

Submitted to Nucl. Instrum. Methods

---

[1] Now at Institut de Física d'Altes Energies, Universitat Autònoma de Barcelona, Spain
[2] Supported by the Direction des Sciences de la Matière, C.E.A., France
[3] Now at University of Pittsburgh, Pittsburgh, Pennsylvania, U.S.A.
[4] Now at ENEA, Palermo, Italy
[5] Now at CERN, 1211 Geneva 23, Switzerland

1   Introduction

Bhabha scattering ($e^+ e^- \rightarrow e^+ e^-$) has been generally used as the reference reaction in $e^+ e^-$ experiments. The rate of such events detected in specially designed monitors is used to measure the absolute luminosity of the colliding beams, found by dividing the number of monitor events by the Bhabha cross section integrated over the acceptance. The cross sections for processes studied in a colliding-beam detector are then determined with respect to the absolute luminosity given by the reference reaction. At LEP energies this technique is used in precision measurements of the Z resonance cross sections, which are essential for the determination of the number of light neutrino species, as well as the Z parameters. The electroweak process $Z \rightarrow e^+ e^-$ creates an interference for such a reference, however, the effect can be limited by restricting the acceptance to low angles where the Bhabha rates are dominated by small values of four-momentum transfer and therefore largely described by quantum electrodynamics (QED). The large cross-section at low angles gives a further advantage of reducing the statistical uncertainty of the reference measurement.

After the first round of electroweak measurements at LEP, a goal of 0.1% was fixed for the experimental precision of the ALEPH experiment's [1] luminosity measurement. The first generation luminosity calorimeter (LCAL) covering 45 to 190 mrad with lead-proportional chambers, was sufficient to reach 0.37 to 0.49% [2, 3] and provided a basis for a more precise measurement. The reduction of the beam vacuum-pipe outer diameter from 15.6 cm to 10.9 cm for the second year of LEP operation made it possible to replace the small-angle tracker (SATR) modules in front of LCAL, near $\pm 2.5m$ from the *interaction point* (IP), with very compact luminosity monitors covering the polar angular regions down to 24 mrad. Installed in a two week LEP shutdown in September 1992, the SICAL calorimeters gave reliable luminosity measurements from the start. The analysis of the first two month's running is reported in [2]. In this article we describe their design, construction and performance.

1.1   *Design considerations*

At LEP the size of the luminous region is small ($\sigma_x \simeq 0.14mm$, $\sigma_y \simeq 0.003mm$, and $\sigma_z \simeq 7mm$) with respect to the scale of the distance to the detectors, thus once the background and detection efficiencies are under control, the limiting source of systematic error in the measurement is given by the error in the acceptance at the lower θ bound. At small angles the lowest order QED Bhabha cross-section is simply:

$$\frac{d\sigma}{d\Omega} = \frac{16 \left(\hbar c \alpha\right)^2}{s} \left(\frac{1}{\theta^4}\right) \tag{1}$$

which integrated over the acceptance gives:

$$\sigma^{acc} = \frac{1040 \ nb \ GeV^2}{s} \left(\frac{1}{\theta_{min}^2} - \frac{1}{\theta_{max}^2}\right) \tag{2}$$

where the polar angular bounds can be defined as radial limits at a defined z-distance from the IP : $\theta_{min} \rightarrow R_{min}$ and $\theta_{max} \rightarrow R_{max}$.

The importance of the knowledge of the absolute position of the radial acceptance limit can be seen by considering the change in the measured cross-section due to a displacement of the inner

radial acceptance bound:

$$\frac{\delta\sigma^{acc}}{\sigma^{acc}} = \frac{2\delta R}{R_{min}} \left(1 + \frac{R_{min}^2}{R_{max}^2 - R_{min}^2} \right). \tag{3}$$

which implies that a desired overall precision of 0.1% requires control of the absolute value of the radial bound to within $30\mu m$ at the distances of SICAL from the IP. This requirement is fundamental to the mechanical design. Radial resolution of an individual electron's impact may be considerably larger than this value.

The measurement of a scattered e^- or e^+ in a colliding-beam experiment is potentially compromised by interactions in the beam vacuum-pipe wall. At 28 mrad in ALEPH an electron traverses 54% of a radiation length before entering the luminosity monitor. Measurement with an electromagnetic calorimeter solves this problem (see ref. [3]). In such a detector a Bhabha scattering usually deposits two back-to-back showers (radiative Bhabha events may produce three or more showers). Although electrons, positrons and γ's are undistinguishable, their secondary interactions in the beam-pipe produce showers which can be well measured. A calorimeter is sensitive to background coming from the production of two (or three) hard photons ($e^+ e^- \rightarrow \gamma\gamma(\gamma)$), but the rate of the process is calculable and low (0.016%) with respect to Bhabha scattering.

The principal source of background to Bhabha scattering at LEP is the accidental coincidence of off-momentum beam particles. The acoplanarity of most of these coincidences is an efficient criterium to separate them from the Bhabha events. Furthermore, their energy spectrum within the calorimeter's acceptance is typically (1992, 1993) peaked between 20 and 25 GeV when running at the Z resonance, whereas the mean accepted Bhabha e^- or e^+ energy is 44.9 GeV. An energy resolution better than $40\%/\sqrt{E}$ is sufficient to separate them from the luminosity events when combined with the acoplanarity rejection.

These considerations, the space available after the removal of the 17 cm long SATR modules, and the experience in ALEPH with the previous luminosity calorimeter defined the essential design requirements :

1. Full containment of 45 GeV electromagnetic showers requires 24 radiation lengths (X_0). Tungsten as a showering material, with twelve samplings using silicon detectors, gives an average radiation length of $5.2mm$ (compared with $3.5mm$ in pure W). This satisfies both space and energy resolution requirements.

2. Precision on the absolute radial fiducial limits of better than $30\mu m$ is needed. The well defined pad boundaries of silicon detectors permit this. Using the technique of comparing the energy sharing between adjacent pads at a boundary to define the cuts, this can be achieved for high density samplers, provided the pad to pad response uniformity is better than 1 to 2%.

3. Understanding of various systematic effects requires good definition of the shower's radial transverse distribution away from the detector's edges. Radial padwiths near half the Molière radius ($R_M \simeq 10mm$ for the material considered) are sufficient for this, since typically 90% of the total energy lies within a cylinder of radius R_M. Such a pad size is also optimized for energy sharing decisions at the fiducial boundaries.

4. An acoplanarity selection to remove off-momentum background requires azimuthal information. A ϕ-padwidth of 11.25° with each subsequent layer shifted in azimuth by 1/3 of

a padwidth ($3.75°$) is adequate for this purpose. A full 2π azimuthal acceptance, without projective cracks, avoids any systematic errors from azimuthal cuts. First order effects from beam-detector offsets can be removed by using asymmetric radial acceptances on either side of the IP and alternating them on a event by event basis.

5. Measurement of trigger efficiency is required for an absolute luminosity determination. Independent triggering on "odd" and "even" layer energy sums gives a cross-check.

1.2 General layout

The luminosity monitor consists of two homogeneous cylindrical silicon-tungsten sampling calorimeters which surround the beam pipe at approximately $z = \pm2.5m$ on either side of the IP. Figure 1 shows a section view of one of the calorimeters. The calorimeters have inner and outer (active) radii of 6.0 (6.1) and 14.6 (14.5) cm, respectively; the active volume subtends the polar angular region from 24 to 58 mrad. Altogether twelve layers of tungsten alternate with layers of silicon detectors, described below. Assembly around the beam vacuum-pipe requires that each calorimeter be divided into two halves (right/left). Each half-calorimeter is stacked using 12 nearly identical minimodules, consisting of an instrumented silicon layer sandwiched between two tungsten plates, described in section 3. The charge amplifiers are described in section 5.1. A motherboard installed at the backplane of each half-module regroups command signals, distributes voltages, and routes the output data. Altogether 12 228 channels are equipped for the two full calorimeters. The mechanical precision of the assembled calorimeter is discussed in section 4.

2 Silicon detectors

The $1.3m^2$ active area required for the two calorimeters is covered using 384 *passivated implanted planar silicon* (PIPS) $300\mu m$ thick detectors manufactured by Canberra Semiconductors [6]. The $33.72cm^2$ sectors ($22.5°$ wide) are cut from 10 cm diameter wafers, shown in Figure 2. They are divided into 2×16 pads with effective dimensions of $5.225mm \times 11.25°$, surrounded by a $100\mu m$ wide guard ring. The flatness of the sectors was required to be within $\pm8\mu m/10cm$. In order to approach the beam-pipe, the inner edge of the sector is cut circularly with a laser, allowing $600\mu m$ between the cut and the guard ring. Low fabrication yields ($\simeq 60\%$) were associated with this cut.

The PIPS detectors are classical diodes, using high resistivity ($\geq 7K\Omega cm$) n-type silicon. The pads and external guard ring were implanted (B^{11}) on the rectifying p^+n junction side, where the photolithography assures a pad reproducibility within $\pm2\mu m$. A $100\mu m$ inter-pad and guard ring spacing ensures no dead zones when the detector is fully depleted. A SiO_2 layer is deposited over the surface, followed by $700nm$ of aluminium over the pads; metallized passages in the SiO_2 allow DC readout of the pads. The noninjecting nn^+ ohmic side (P^{31} doped) is overlayed with $300nm$ of aluminium allowing connection of the polarization voltage. The detectors are sufficiently reverse-biased, typically 35 V, to fully deplete the silicon bulk, as shown in Figure 3. Depleted detector capacitance C_{det}, shown in Figure 4, varies linearly with padsize from 25 pF to 55 pF. The dark currents, measured for the final detectors, are typically less than 5 nA per pad, where production specifications required dark currents less than 20 nA/pad and/or less than 100 nA for any 5 pads on the crystal.

In order to obtain the thinnest possible silicon detector units, a front-surface readout approach was initally explored. Prototype $300 \mu m$ thick crystals were prepared with DC coupled aluminium readout lines deposited over a $5 \mu m$ thick polyamide insulator covering the pads (two companies developed prototypes [7, 6]). The approach was abandoned because of project delays after difficulties with unstable operation due to coupling between read-out lines and the guard ring, cross-talk between pads via the lines, and channel failures due to the fragility of contacts between readout lines and the pads. The adopted solution described below uses printed circuits on a kapton foil bonded to the detector p-side.

CESIKA detector sub-assemblies. The individual silicon detectors are mounted on ceramic supports which position them around the half disk of each mini-module (discussed in the next section). The silicon and ceramic wedges are equipped with $180 \mu m$ thick double-sided printed Kapton readout circuits to form ceramic + silicon + Kapton (CESIKA) sub-assemblies. First, Ag-loaded conductive epoxy [8] is used to bond the ohmic side of the silicon detector on to the $635 \mu m$ thick gold-plated ceramic support. A ceramic jig, with a similar thermal expansion coefficient, is used to align the silicon detector with the help of a video-microscope. Curing of the assembly requires 2 hours at 120°C. Optical measurements after curing give a radial precision of $9 \mu m$ r.m.s. (consistent with the measurement precision) between a positioning hole in the ceramic and the pads on the crystal. Second, a Ag-loaded epoxy is used to bond the Kapton readout circuit onto the metallized pads, shown in Figure 5. The reliability of this contact was tested on prototypes with accelerated aging methods. The Kapton circuit is attached to the front-end electronics card via a connector. Mechanical and electrical tests are performed before mounting the CESIKA unit.

3 W-Si-W minimodule construction and calorimeter assembly

Each of the 12 minimodules forming a half-calorimeter sandwich eight silicon detectors between a thin (front) and a thick (rear) tungsten radiator, giving a radiation sampling length of $1.95 X_0$. An additional W plate is bonded onto the front face of the first minimodule so that its sampling thickness is the same. In order to ensure the highest possible detector density, the instrumented gap between the W plates is limited to 2.33 mm, as shown in Figure 6. Minimodules differ only because of the successive azimuthal offsets ($+3.75°$, $0°$, and $-3.75°$) used to avoid aligned cracks and to improve the ϕ resolution.

An alloy was used for the tungsten radiators [4]: 97.0% W, 1.6% Ni, 0.8% Fe and 0.6% Cu, with a resulting density of $18.98 g/cm^3$. This choice simplified the machining of the plates to the desired uniformity and flatness. The W plates, machined as full disks, are cut in two halves with an angled cut of $36°$ with respect to the surface. This ensures that there is no projective discontinuity at the junction of two plates, as shown in Fig. 7.

The rear W plate of a minimodule, 3.8 mm thick, is bonded to an epoxy-fiberglass "G-10" plate, which serves both to hold the entire assembly on the support rods as well as to locate the silicon detectors. The dimensional stability of the G-10 plate is critical to the overall precision. The material was chosen for its thermal and hydroscopic properties [5]. Two 16.5 mm diameter precision holes allow the G-10 plate to slide onto support rods at the stacking stage. Each CESIKA unit's ceramic support is referenced with a 3 mm diameter precision pin ($5 \mu m$ hole tolerance) and held in a slot machined in the plate (edge precision is obtained by molding).

The coordinates of all the alignment holes were measured at $20°C$ with a precision of $5\mu m$ using a computerized scanning table [9]. The values were entered into a database for analysis purposes; the azimuthal position of the holes agreed to within $\pm0.01°$ with the design. Subsequently, it was found that the *in situ* operating temperature is $8°C$ higher (typically $28°C$ $\pm0.3°C$ r.m.s.) than was used for the measurements of the reference holes. The thermal expansion coefficient of the bonded pair of G-10 and W-plates was measured and found to be isotropic, with $\alpha_T = (8.0\pm0.3)\cdot10^{-6}/°C$. This gives an increase of the inner diameter of $(9 \pm 3)\mu m$ with respect to the measurements at $20°C$, including the expansion of the ceramic supports and silicon detectors.

The CESIKA detectors overlap at alternate depths around the G-10 plate: a 0.20 mm depth difference minimizes azimuthal variations (see sect. 7.2). The overlap with the neighboring silicon detector is centered between the pad edge and the guard ring. The edge of the underlying detector is shadowed by the 1.5 mm of silicon extending beyond the pad. This shadowing is constant with radius and thus unimportant for the luminosity measurement. Once positioned on the plate, the CESIKA units are equipped with the front-end amplifier cards.

The front W plate of a minimodule, 3 mm thick, is bonded to a thin aluminium plate (machined to 0.5 mm in the region of the W) with which it is held on the support rods. Silicon PTC temperature probes are placed on the front aluminium-W plate near selected pre-amplifier chips. This plate is also used to make thermal contact with the water-cooling system. A platinium (PT100) probe is positioned on the central W-plate of each half-calorimeter.

The two plates of the equipped minimodule are screwed together around the edge via the G-10 and aluminium plates.

The calorimeter is assembled by stacking the minimodules together on the 16.5 mm diameter stainless steel support rods, located 10 cm from the tungsten outer edge, see Figure 8. The tolerance of the fit on the rods is $10\mu m$. The support rods are maintained parallel by the aluminium calorimeter case, which when closed acts as a Faraday cage to isolate the detector from possible noise generated by other ALEPH sub-detectors. The motherboard and auxilary electronics are mounted on the 8 mm thick aluminium rear plane of the calorimeter. The last W-plate, which is located after the final silicon sampling layer protects the detector from rear entering soft gammas and ensures the same back-scattered component of the shower sampling as seen by the other layers.

The calorimeters are supported on $30mm$ diameter horizontal stainless steel rods fixed to the ALEPH central detector (TPC) support legs, orthogonal to the beam-axis. The silicon detectors are protected against synchrotron radiation coming through the vacuum-pipe wall by a 2 mm thick lead tube placed around the beam-pipe before closing the modules. The half-calorimeters are then slid into position on either side of the vacuum-pipe.

4   Mechanical stability and precision

Once installed, a geometrical survey gives the absolute position of each module within $\pm0.2mm$ in x and y, and $\pm0.5mm$ in z (along the beam axis). The relative separation between half-calorimeters is measured by 4 groups of light emitting diodes (LED) and photodiode receivers, giving a precision of $8\mu m$, calibration uncertainty included. The separations are continously monitored during the data taking; the maximum drift during a year's data taking was less than $8\mu m$. Additional LED groups are installed between the TPC and the leg supporting the SICAL to monitor movements of the calorimeters along the beam direction, in particular, with the turn-on of the 1.5 Tesla magnetic

6

field. The z-positions of both calorimeters over the 5 m distance are stable with respect to the survey positions within a mesaurement precision of $100\mu m$.

Internal mechanical stability depends upon the thermal stability of the detector. The total power dissipation is 70W per half-module. Water cooling (temperature stabilized) is sufficient to maintain a constant temperature within $\pm0.3°C$, thereby keeping the silicon detector radial positions within $\pm3\mu m$.

The various sources of the uncertainty on the silicon detectors' absolute mean radius are summarized in Table 1. A total radial uncertainty of $9\mu m$ is found ($18\mu m$ given in [2] was prior to measurements of α_T for G-10 plates, described previously). It assumes that the errors related to individual silicon detector units, (1), (2) and (3) in Table 1, are reduced by the luminosity measurement in the 16 CESIKA units in azimuth per layer. The minimodule errors, (5) and (6), are reduced by $1/\sqrt{2}$, since two layers are used together for the fiducial selection. Finally the overall error is reduced by combining two independent selections using either endcap calorimeter to define a tight fiducial cut. Only the thermal effect is considered to be coherent between both sides.

5 Electronics and readout

5.1 *Charge amplifiers*

The charges collected from the individual pads of each silicon detector are integrated using a pair of 16-channel "Application Specific Integrated Circuits" (ASIC), each serving half of a crystal in azimuth. The ASIC includes preamplifiers, shaping amplifiers, track-and-hold circuits, a fast-OR for triggering purposes, an internal calibration circuit and digital readout switches. It is based on the CMOS AMPLEX chip developed by CERN for the UA2 experiment's silicon track detector; the present version, adapted for calorimetry purposes and including the trigger and calibration upgrades, is called the AMPLEX-SICAL [10, 11]. The chip specifications and performance are summarized in Table 2. Its radiation tolerance, up to about 250 Krad, is largely sufficient for use at LEP. A schematic diagram is shown in Figure 9.

The principal modifications in the AMPLEX ASIC which were required for the calorimetry application were: (1) the extension of the dynamic range to 1000 Mip for each channel ("Minimum ionizing particle", where 1 Mip in the $300\mu m$ thick silicon detector gives $\simeq 22Ke^-$'s, ref. sect. 7.1), (2) the addition of a fast-OR (in PRESET mode), where the output is the analog average of all 16 channels, and (3) the addition of an internal calibration circuit permitting charge injection via 2 pF (externally calibrated) capacitors, with MOS command signals to allow selection of individual channels.

The amplifier response is linear within 1% over the full dynamic range. Corrections to the residual non-linearity are made using a parabolic parametrization fit to the output signals. The gain of individual channels increases linearly due to the internal layout from channel 1 to 16, typically within a full range of 2%. Since the amplifier gain depends upon C_{det}, $-0.35\%/pF$, an additional channel to channel variation is present due to the radial C_{det} dependence of the silicon detectors. The implimentation of the chip was arranged to partially counterbalance these two effects. The net effect is removed from the data by calibration. The noise also depends upon the

detector capacitance:

$$Equivalent\ Noise\ Charge = 800e^- + \left(38e^-/pF \times C_{det}(pF)\right).$$

which amounts to $\simeq 0.2$ Mip for the silicon detectors used. This gives an overall noise < 1 ADC count for the complete electronic chain. The output depends upon the HOLD timing, as shown in Figure 10a. The hold timing in the acquisition mode is adjusted so that the maximum pulse height is obtained for the total energy seen in both calorimeters with coincidence triggers, typically $250ns$ after beam crossing. In calibration mode, the same hold timing with respect to charge injection is obtained by maximizing the output signal when injecting 1 V on two channels (3 and 4) of the AMPLEX chip. The analog buffering of the shaped signals ensures a signal drop < 1 ADC count over 10 ms, insignificant over the acquisition time scale. A signal on a single channel typically induces a -1.6% cross-talk ($250ns$ HOLD delay) over the other outputs, via the chip substrate. This can be modified by the detector capacitances and adjacent pad coupling. Figure 10b shows the cross-talk for adjacent pads and for a more distant pad on the same crystal. The effect of positive cross-talk for late HOLD values can be seen for full showers summed over many channels from LEP data (shown in Figure 10a). This behavior has been studied in the light of LEP bunch-train operation where beam bunch separations from 200 to $500ns$ are considered.

The AMPLEX chips are mounted by pairs on front-end cards which are DC coupled via the kapton foil (ref. Figure 5) to the pads of a single crystal; each chip serves the 16 channels of an $11.25°$ ϕ-slice. The card distributes power for the chips (decoupled from the power supplies). the bias voltage for the crystal, and includes a protective $100K\Omega$ resistor to measure the reverse-current. Typical power consumption is 400mW per card. An external calibration permitting rapid checkout of the complete chain is included on the card using capacitive coupling between the amplex input signals and a common injection line for 8 inputs. The card receives command signals from the motherboard and uses 4 analog switches to control the charge injection for both internal and external calibration.

The motherboard installed at the back-plane of each half-calorimeter adapts and distributes command signals from the sequencer to all amplex cards via a daughter command-card, and routes the output data to 24-channel daughter data-cards (each serving 12 layers at the same azimuth). Partially shielded flat cables (25 pin) connects the front-end cards to the motherboard, where the shielding was added to reduce cross-talk between the AMPLEX command signals and neighboring cards output signals.

The differential output front-end signals are buffered and sent to the electronics barracks via 30m 25-pair shielded cables. Level adaptors, at the barracks, receive the differential outputs and perform two functions: (1) shift the output levels by +2 V to match the input range (-0.4 to 4.6V) of the multiplexed analog to digital converter (MUX-ADC, described in the next section), and (2) send a second output to the trigger electronics.

Common grounding to the experiment is made for data outputs at the MUX-ADC Fastbus crate level, and at the trigger Fastbus crate level for the trigger signals.

5.2   MUX-ADC's and sequencer

The analog signals from the front-end electronics are digitized with multiplexed input 12 bit voltage level digitizers, Fastbus F6845 MUX-ADC, designed for the ALEPH electromagnetic calorimeter

(ECAL). The readout and multiplexing is synchronized with a programmable sequencer, MUX-SEQ. Each MUX-ADC receives the information from 2 daughter data-cards on the calorimeter's motherboard (described above). corresponding to all 12 layers of four azimuthal consecutive sectors. where the signals from the level adapters arrive via a data board on the auxilary backplane. The full range of the level adapted output signals was chosen large enough such that the ADC is never saturated for electromagnetic showers from a Bhabha event. The full dynamic range is slightly reduced by the pedestal values: typically $\simeq 300$ ADC counts out of 4095 (full range).

Although each MUX-ADC module contains 12 ADC chips processing in parallel, only 6 are used for this application. Inputs to these chips are multiplexed serially by a factor 8. The individual ADC signal conversion time is 6.875 μsec, where each AMPLEX provides 16 pad signals and 1 fast-OR signal to be digitized serially. Altogether the total conversion time. including front-end initialization sequence, takes $\simeq 1$ msec for the calorimeter.

A fast hardware "zero suppression" algorithm is implemented in the MUX-ADC's which permits a substantial reduction of the readout volume. Triplets of pad energies (same radial and azimuthal bins in subsequent layers) are compared against their corresponding reference thresholds; all three pads of a triplet are read out if one of them is above 4 ADC counts ($\geq 20 MeV$). The triplet structure. internal to the MUX-ADC, comes from the original ECAL application. Zero-suppression of the whole calorimeter is performed in $200\mu sec$.

The Fastbus F6846 MUX-SEQ module is a programmable sequencer with an 8 MHz clock used to synchronize the readout and multiplexing of the front-end electronics with the MUX-ADC's. In addition, it sends the command signals in both acquisition and calibration modes, as well as the calibration pulses to the front-end electronics for detector checkout and calibration. It also conforms to the trigger protocol convention used for the various DAQ configurations. An auxiliary sequencer board distributes the ECL differential command signals to the four half-calorimeter module daughter command-cards.

5.3 Data-acquisition

In order to ensure a common dead time between the luminosity measurement and the hadronic event collection, and in order to use the added acceptance provided by the calorimeter for Z decay products (for example) at small angles, the readout is included in the general data-acquisition system as for any of the other sub-detectors. This follows the treelike architecture of the existing system where the luminosity event information is combined with the information coming from the other sub-detectors into a single event. The event building process accesses the formatted information in the event buffer of the SICAL Event Builder (EB), operating under OS-9.

The detector's DAQ is based on the Fastbus standard. Two Fastbus crates are used: one reads out the front-end electronics and the other implements the trigger decision (described in sect. 6). The readout crate contains 16 F6845 MUX ADC's, one F6846 MUX Sequencer to drive the ADC's. and an Aleph EB 6858F, used as Fastbus master. In addition. a crate clustering card (CCC) F682E and segment interconnect (SI) are required.

Readout functions are defined as 3 independent tasks: producer. reformatter and consumer. The producer initializes the DAQ (loads the sequencer program and the thresholds into the ADC's). reads the digitized zero-suppressed information from the ADC modules and puts the raw data into the event buffer. The procedure is optimized to reduce the event readout time, which, at low trigger

rates, defines the SICAL dead time, presently limited to about 7 msec.

The reformatter performs the pedestal subtraction of the data and prepares a formatted event consisting of several banks containing calorimeter hits and trigger information to be sent to the data stream. The average SICAL event size for Bhabha events (typically 120 hits) is 5 Kbytes, raw data after reformatting.

6 Trigger

Three trigger types are required for the luminosity measurement: a double-arm coincidence trigger (SCAL-MED), a very-high threshold single-arm trigger (SCAL-HI) and a very-low threshold single-arm trigger(SCAL-LO). In order to measure the efficiency, each trigger type is formed using redundant, independant triggers derived separately from the odd or even planes by summing the pad energies within $45°$ azimuthal segments. Trigger characteristics are summarized in Table 3. In contrast to the other sub-detectors, the SICAL triggers are fully formed within the sub-detector's own trigger system. The final luminosity trigger logical levels are sent to the general Level-1 trigger (decision within about $5\mu sec$), thereby respecting the readout protocols.

The double-arm coincidence trigger is required to be 100% efficient for Bhabha scattering events while giving good rejection of background from accidental coincidences of off-momentum beam particles. It demands the coincidence of a "localized" high energy deposit, A_{high} or B_{high} (typically $\geq 24GeV$) in endcap calorimeter A or B respectively, with a similar deposit above a less stringent threshold, B_{low} or A_{low} (typically $\geq 12GeV$), in the other endcap. The coincidence, $(A_{low} \cdot B_{high}) + (A_{high} \cdot B_{low})$, is an OR of four conditions:

$$\left((A_{low}^{odd} \cdot B_{high}^{odd}) + (A_{high}^{odd} \cdot B_{low}^{odd}) \right) \text{ OR } \left((A_{low}^{even} \cdot B_{high}^{odd}) + (A_{high}^{even} \cdot B_{low}^{odd}) \right) \tag{4}$$

$$\left((A_{low}^{even} \cdot B_{high}^{even}) + (A_{high}^{even} \cdot B_{low}^{even}) \right) \text{ OR } \left((A_{low}^{odd} \cdot B_{high}^{even}) + (A_{high}^{odd} \cdot B_{low}^{even}) \right). \tag{5}$$

The very high threshold (typically $\geq 39GeV$) single-arm trigger is used to cross-check the coincidence trigger efficiency.

The very low threshold single-arm trigger (typically $\geq 9GeV$) provides information on the off-momentum beam particle spectrum, used to estimate the contamination to Bhabha scattering. It is substantially downscaled (ref. Table 3) to reduce its impact on the experiment's dead time, allowing enough statistical precision for the background estimate.

Each trigger sector is designed to contain the full energy deposit of an e^-, e^+ or a γ, thus $45°$ sectors (octants), corresponding to two silicon crystals, were chosen. In order to properly handle showers overlapping a border between two octants, two separate trigger sector sub-divisions are used: "Road 1" and "Road 2", rotated in azimuth by a half-octant with respect to each other, as shown in Figure 11. Since the trigger signals are summed over ODD or EVEN layers, altogether 64 sectors are used including both endcaps.

6.1 *Trigger electronics*

The trigger system is built using two dedicated Fastbus cards: the MIXER sum cards, 8 per endcap, and a single Total sum card. The fast-OR analog signals from each endcap are transmitted

to the trigger system via the level adapters. The MIXER sum cards digitize the signals with flash ADC's, and then form independent Road 1 and Road 2 digital sums for the odd and even plane sectors as described above. A group of 4 Mixer sum cards forms a summing network to prepare the 16 sector sums for a single endcap and parity (odd/even). The final double-arm and single-arm triggers are constructed on the Total sum card. Field programmable gate arrays (XILINX [12]) are used throughout the system to make and manipulate the digital sums. The final SICAL trigger decisions are sent as ECL signals to the main trigger. The total time needed to make these decisions is about $1.5\mu sec$, where all but about $250nsec$ is in cable delays.

MIXER sum cards. A block diagram of the mixer, based upon 5 XILINX gate arrays, is shown in Figure 12. Each card's primary inputs serve either the first or last 3 odd/even layers of four adjacent trigger sectors (Road 1 or Road 2). AC coupled inputs avoids large DC-offsets. The input signals are converted with AC-coupled 7-bit (25 MHz) flash-ADC's [13] (48/card). The digitization timing is defined by a command from the Total sum card derived from the Gated beam crossing. Only the 5 highest bits are used for the sums (the lowest 2 serve for testing). In the case of noisy channels, individual flash-ADC's may be disconnected via Fastbus.

Once the input signals have been digitized, the Mixer cards form trigger sector sums in two steps in order to share the information from adjacent sectors. First, the four XILINX on each card form intermediate sums with the signals digitized on the card. Then each XILINX forms a total sum for the trigger sector it represents (Road 1 or 2, odd/even). The remaining offsets measured during pedestal runs are subtracted from the final sum in each XILINX. The total sector sum has a dynamic range of 256 ADC counts, with an overflow bit. A 45 GeV shower typically gives a sector sum of 50 ADC counts.

Finally, the pedestal-subtracted sector sum is compared against the four programmable thresholds described above in the fifth XILINX on the Mixer sum card. The four discriminator masks on a single card are pre-OR'ed and the result is sent to the Total sum card.

Total sum card. The trigger masks from the Mixer sum cards of both endcaps are ORed together in a single XILINX on a Fastbus Total sum card. The 6 basic triggers (ref. Table 3) are generated from the 12 conditions described above and sent to the main trigger, they can also be readout from the card for analysis purposes. At the main trigger these 6 are OR'ed to generate the three SICAL triggers: very low (SCAL-LO), coincidence (SCAL-MED), and very high (SCAL-HI), each of which can be separately downscaled.

The card "handshakes" with the main trigger supervisor in data acquisition mode: all trigger signals remain high until a level-1 decision (YES/NO) is made, at which point the signals drop. This avoids programming fixed delays into the trigger electronics and guarantees that the Total sum card respects the general protocol.

6.2 *Trigger calibration, rates, and performance*

The trigger energies are calibrated using Bhabha events from the data. The trigger total sums are compared against the MUX-ADC energies read out for the same events, as shown in Figure 13. A linear fit is made for each trigger sector for every LEP fill. The resolution of the trigger electronics is 4% for the six (odd/even) planes, which is small compared to the calorimeter resolution. The noise of a single sector, due essentially to the front-end electronics, is typically 1 GeV.

Typical rates for a LEP luminosity of ($1 \cdot 10^{31} cm^{-2} s^{-1}$) are shown in Table 3. These depend

11

both on luminosity and background conditions. Clearly the very high single-arm triggers generally satisfy the coincidence condition, therefore their exlusive rate is typically low (120mHz for the conditions shown). Background studies using the very low single-arm triggers from the 1993 data sample show a accidental double-arm coincidence contamination of $7 \cdot 10^{-4}$, underlining the low background of the LEP beam at ALEPH during that period.

The coincidence efficiency is shown in Figure 14 versus the energy in the arm opposite to the very high single-arm trigger, where events from Bhabha scattering should satisfy both trigger conditions. The efficiency turn-on is clearly visible above the low threshold at 12 GeV. The coincidence trigger is fully efficient, 100%, above 20 GeV. The odd versus even layer trigger efficiencies give very tight limits on their relative inefficiency: $< 10^{-4}$, and the overall inefficiency of their OR used in the final trigger is completely neglible.

7 Performance studies

Most of the detector's performance requirements for luminosity measurement can be evaluated using Bhabha events collected at LEP; this was important since the tight construction schedule only allowed for prototype tests of critical performance aspects with at most only a partially complete detector. We describe here the test beam measurements of the peak charge collected on the final design silicon pads as a function of shower depth and incident beam energies, necessary for the AMPLEX redesign. The linearity of the amplifier over the range covered, ensures the calorimeter's linearity to sufficient precision. Test beam studies of shower response as a function of air-gap separation at the silicon layers give some insight into azimuthal variations observed in the LEP running. The essential measurements, performed with a final detector prototype and a silicon-strip tracker, to determine the energy sharing asymmetry at the pad boundary are described, and compared with LEP data. Full shower developement in the detector is shown using LEP data. The detector's uniformity and stability are shown using the data collected in 1992 and 1993 at LEP.

Concerning the operation at LEP, it should be remarked that the detector has shown no clear sign of radiation damage in the two and a half year's running. No loss of channels has occured during the running periods. Furthermore, noise levels, as indicated by pedestal studies, are stable over two years' running. Clearly, estimated radiation levels at the detector faces have been low, $\leq 300 rad/year$. Two AMPLEX cards out of the 384 have occasionally become noisy, typically cured by cycling the low voltage. The first appearance of the effect, in coincidence with a beam loss, lead to a conservative running procedure, whereby the silicon detector reverse bias voltages are set to zero during LEP beam injection and adjustments. The front-end amplifier voltages are kept on to ensure the detector's temperature stability.

7.1 *Single pad MIP and maximum response*

In order to define the design parameters for the calorimeter version of the AMPLEX ASIC (ref. sect. 5.1) measurements were made of the largest single pad response to electron showers. A tungsten prototype with a single silicon detector was used, reading out only one pad with the beam centered on it. The shower profiles were determined by varying the thickness of tungsten in front of the silicon, with $\geq 4.5 X_0$ behind to keep backscattering effects constant. A scintillator

telescope defined the incident particles. and a $1m$ thick iron absorber followed by a counter tagged muons. Measurements with 70 GeV muons defined the energy deposit for MIP; the most probable energy deposit in the $300\mu m$ thick fully depleted silicon detectors gives $1MIP \equiv 3.6fC$. Electron beams of 35, 50, 70 and 100 GeV were used to study the longitudinal profile. Figure 15 shows the comparison between the test beam results in a 50 GeV electron beam and data taken at LEP with the final detector. Figure 15a shows the energy distribution at $6.5X_0$. As an estimator, a Gaussian was fitted to the peak of the response curve. The most probable value is shown versus shower depth in figure 15b. The continuous curve is the best fit to the test beam data with a function of the form:

$$Q = q_0 t^a e^{-bt}.$$

where t is the thickness in X_0. The points are the results for Bhabha events at LEP. The design limit for the AMPLEX was determined using the 100 GeV data; the peak charge on a single pad at shower maximum was $2250fC$. A limit charge of $3.8pC$ was conservatively chosen to allow for shower fluctuations, and variation of pad size.

7.2 Single pad response versus Si-W separation

The silicon detectors in the final detector are alternately overlapping in azimuth. In order to investigate the sensitivity of the response to variations of the air gap between the layer and the tungsten in front of it, a study was made using a single detector element placed behind $5X_0$ of tungsten, followed by $7X_0$. The results for an incident 50 GeV electron beam are shown in Fig. 16, showing a -5%/mm loss.

In addition to the absorption of soft electrons in the air gap, reducing the signal in the silicon as the space increases, the absorption of backscattered shower constituents from the following tungsten plate is also expected in the G-10 plate supporting the detectors [14]. Since the support plate thickness is staggered in azimuth to permit the overlap of the detectors, the two effects are opposed. A 4% shift of the total energy between alternate silicon detectors, observed at LEP, is assumed to result from the combined effect.

7.3 Radial transverse energy distribution

Shower containment defines the detector's useful fiducial volume. The radial transverse distribution for a single azimuthal padwidth at a depth of $8X_0$ (shower maximum) is shown in Figure 17 for LEP data centered (a) on a pad boundary. (b) on a pad center. Essentially full containment ($\geq 95\%$ of the energy) extends from the third radial bin from the calorimeter edge. consistent with the expected R_M. A typical 45 GeV electromagnetic shower within this volume deposits its energy over the full depth in 80 to 100 pads ($E_{pad} \geq 10 MeV$) depending inversely upon the incident radius.

7.4 Radial energy asymmetry versus depth

Radial fiducial selections of events in the calorimeter. essential to the luminosity measurement. are based upon radial energy sharing between adjacent pads. The radial energy asymmetry A_r is

defined by:

$$A_r = \frac{E_{in} - E_{out}}{E_{in} + E_{out}}. \tag{6}$$

where E_{in} is the energy inside a radial padwidth within the fiducial region and E_{out} is the energy in the adjacent padwidth outside the region. Figure 18 shows the typical A_r variation with radius near the pad boundary. The luminosity systematic uncertainty $\delta\mathcal{L}/\mathcal{L}$ depends upon the radial dependence of this asymmetry at the fiducial boundary, and is given by the formula:

$$\frac{\delta\mathcal{L}}{\mathcal{L}} = \frac{2f}{R_{min}} \left((dA_r/dr)^{-1} \delta A_r \right) \tag{7}$$

where f is a geometrical factor depending upon the inner and outer fiducial cut radii (f=1.24 for the Bhabha selection outlined in sect. 7.7) and $\delta A_r = 1/2(\delta E/E)$, the cell-to-cell energy uncertainty.

A second test beam prototype, with a final design silicon sampling layer (minimodule, ref. sect. 3) was used to measure the dA_r/dr slope at the pad boundary as a function of shower depth. The measurements were performed for four silicon sampling layers, with an incident 50 GeV electron beam. The incident electron trajectory was defined using $16 \times 20cm^2$ silicon strip detectors (2 mm strips) adapted from the NA14 silicon active target [15], positioned 30 cm upstream of the prototype. The strip detectors were arranged as a telescope, two groups for x and two for y, with staggered planes such that the effective resolution for a track in four x or y planes was $(500/\sqrt{12})\mu m$. A scintillator telescope defined the latch timing, and a veto counter was placed $40 X_0$ behind the prototype to remove muons. The beam spot at the calorimeter face was 12 mm r.m.s. in x and y, which accepted tracks crossing two pad boundaries of the prototype at the same measurement point. The precision of the pad geometry was used to cross check the extrapolated track position.

The results for fully contained showers near the boundary between radial pads 4 and 5 are shown in Fig. 19, where the inverse of the fitted slope, $(dA_r/dr)^{-1}$, at the pad radial boundary is plotted versus shower depth for single pads. The increase of shower width causes $(dA_r/dr)^{-1}$ to increase with depth as expected.

Also shown on Figure 19 are asymmetry slopes for LEP data. Since there is no tracking detector in front of the luminosity calorimeter at LEP, we have used the "non-projective" geometry of the detector to constrain the extrapolated shower centroid. Energetic showers (mean energy of 44.9 GeV) are selected if the centroid in one of the adjacent layers is near the radial pad boundary (pads 4 and 5), obtained by requiring that $A_r \to 0$ for that layer. The extrapolated centroid is determined from this position and the beam IP, using the known geometry of the layers. The asymmetries in adjacent layers for the same showers are fitted against each other using the extrapolated position information to extract the slope versus layer shown in Figure 19. Small radial corrections (O(10 to 25μm)) due to pad curvature are not taken into account here since only the differences in these between layers enters in the extrapolations. The $(dA/dr)^{-1}$ slope in the first layer (2 X_0) is wider for the LEP data compared to the test beam; an EGS simulation including the ALEPH solenoid's 1.5 Tesla B-field shows the same effect, due to preshowering in the beam pipe 70 to 80 cm upstream.

This study shows that an acceptance cut based upon asymmetry selections from samplings at depths of 6 to 8 X_0 would have a radial precision of $\leq 20\mu m$ for a single pair of pads if the stability of the asymmetry measurement (δA_r) is $\leq 1\%$. The final luminosity precision from this dispersion will be reduced by the large number of measurements in azimuth (2×32 pads).

14

7.5 *Longitudinal profile and upstream material*

The advantages of fine segmentation of shower information can be seen in the calorimeter's use to understand the distribution of upstream material. Entering particles must first traverse the aluminum beam-pipe at small angles (24 to 58 mrad) and then pass through a background monitor (SAMBA $\simeq$ 2% Xo). The total thickness traversed varies smoothly from 54% Xo at 28 mrad (inner fiducial cut) down to 34% Xo at 48 mrad (outer fiducal cut), excepting locally for two beam-pipe support rings ($\simeq$ 12% Xo). The Bhabha event longitudinal shower profile shown in Figure 20a is used to study the variation of material with incident angle.

Figure 20b shows the relative mean shower depth versus polar angle for both the A-side and B-side calorimeters. The increase with angle agrees well with the measured beam vacuum-pipe wall thickness. A beam-pipe support ring ($0.12 X_0$ thick) can be seen only on the B-side, since it was permanently removed on the A-side to allow installation of the silicon vertex detector.

7.6 *Energy uniformity and resolution*

The uncalibrated detector uniformity is $\simeq$ 3.8%, most of which is due to the dispersions of the AMPLEX chips (re. sect. 5.1), found to be stable over a year's running. Periodically the response of each AMPLEX is measured by individually pulsing all channels. The average gain (parabolic fit over 5 injected levels) and relative interchannel slope per chip are sufficient to yield residuals below 0.7%, thereby reducing the number of constants for the 12288 channels from 36864 to 3856.

Applying the calibration constants, and accounting for the observed 4% shifts in alternate silicon detector response due to the different air-gap and support thicknesses, yields an energy resolution of 4.9% for fully contained 45 GeV electromagnetic showers (LEP data); $\sigma_E/E = 34\%/\sqrt{E}$.

7.7 *Luminosity measurement*

A description of the luminosity analysis of the 1992 data and the systematic uncertainty in the measurement is given elsewhere [2]; in this section the selection procedure is outlined and used to show the detector's efficiency to remove the off-momentum background. The stability of the luminosity measurement is shown in a comparison with the number of hadronic Z decays collected by ALEPH during the same runs.

The Bhabha scatterings (typical event shown in Figure 21) are selected from luminosity co-incidence triggered events by requiring at least one reconstructed cluster in each endcap with an energy $\geq$ 44% of the beam energy ($\geq$ 20 GeV at the Z peak). Their sum must exceed 60% of $\sqrt{s}$ ($\geq$ 55 GeV at the peak) to remove the off-momentum beam background from the Bhabha scatterings. Figure 22 shows the typically clean separation obtained between the Bhabha peak and the off-momentum background. Radial fiducial cuts (one cluster within a "tight-acceptance", and the opposite within a "loose-acceptance") based upon the energy sharing asymmetry described previously, are used to define the accepted cross-section. The tight and loose cuts are alternated for each event to reduce the sensitivity to displacements of the luminous region. An acoplanarity cut based upon the two cluster's azimuthal difference, $150° \leq \Delta\phi \leq 210°$, is used to remove the remaining off-momentum beam background without severly cutting away the radiative Bhabha

events. Figure 23 shows the typical distribution with the low background conditions in 1993.

A cross-check of the stability of the luminosity selection can be seen in Figure 24 where the ratio of Bhabhas (background subtracted) to TPC-selected hadrons is plotted versus fill number. The ratio is constant within the statistical precision of the points.

8 Conclusions

Since its installation in September 1992, the silicon-tungsten calorimeter has shown itself well adapted to the goals fixed for the luminosity measurement; analysis of 0.74×10^6 Bhabha events collected during the two month running period in 1992 gave an estimated experimental precision of 0.15% [2], limited by the statistics of the Monte Carlo simulation. Considerably more data collected in 1993, 6.4×10^6 luminosity events, has confimed the reliability of the detector and allowed more refined systematic studies, which should give an experimental precision $\leq 0.1\%$. The ultimate limit of the absolute luminosity measurement is defined by the knowledge of the absolute radial position of the silicon pads used for the fiducial selection and the absolute distance along the beam-axis between the two calorimeters, yielding somewhat better than 5×10^{-4} for the detector described here. This is substantially better than the current theoretical 0.25% uncertainty of the Bhabha scattering cross-section evaluated by Monte Carlo generators [16], although efforts are underway to reduce this error [17] to between 0.09 and 0.16%.

9 Acknowledgements

References

[1] D. Decamp et al., Nucl. Instru. and Meth. A294 (1990) 121.

[2] D. Buskulic et al., Z. Phys. C 62 (1991) 539.

[3] D. Decamp et al., Z. Phys. C 53 (1992) 375.

[4] Tungsten D185, Plansee, Reutte, Austria.

[5] ME730 epoxy-fiberglass, Societé Permali, Maxeville, France. The linear thermal expansion coefficient α_T is $1.3 \cdot 10^{-5}/^\circ C$.

[6] Canberra Semiconductors N.V., Olen, Belgium.

[7] Eurisys Measurements (previously Enertec-Intertechnique), Lingolsheim, France.

[8] Epotecny, Pontoise, France.

[9] S.T.C. Societé, Malakoff, France.

[10] E. Beuville et al., *IEEE Trans. Nuclear Science* **39** (1992) 766;
E. Beuville et al., *Nucl. Instrum. and Methods* **A288** (1990) 157.

[11] MEITEC N.V., Oudenaarde, Belgium.

[12] XILINX field programmable gate array, model XC 3064 (70 MHz toggling frequnecy).

[13] Motorola 7 bit, 25 MHz converter, MC 10321.

[14] H. Hirayama, *Proc. IEEE Nucl. Sci. Symposium*, Orlando, Fla. (1992) 254.

[15] R. Barate et al., *Nucl. Instrum. and Methods* **A235** (1985) 235.

[16] W. Beenakker and B. Pietrzyk, *Phys. Lett.* **B304** (1993) 366.

[17] B.F.L. Ward, S. Jadach, E. Richter-Wąs and Z. Wąs, "Precision Calculation of the Small Angle Bhabha Cross Section", *1994 Rochester Conf., Glasgow Preceedings* (1994).

(1) Silicon pad relative to CESIKA alignment hole	9 μm
(2) Alignment pin, CESIKA and G10 hole tolerances	5 μm
(3) Alignment hole position on G10 support	5 μm
(4) G10 support thermal distortion effects	3 μm (16 μm)
(5) Support rod and hole tolerance	10 μm
(6) Support rod hole position on G10 support	5 μm
(7) Half-calorimeter separation LED precisions	5 μm
(8) LED sensors calibration uncertainty	8 μm
Total uncertainty of mean radius	9 μm (18 μm)

Table 1:   Summary of silicon detector absolute radial uncertainties. Values in parenthesis ( ) were used in the 1992 luminosity analysis [2]. Total uncertainty is defined with respect to the final fiducial selection.

Chip technology	3μm CMOS
Number of input channels	16
Full dynamic range	3.8 pC (1000 MIP)
Equivalent noise charge ($C_{det} = 50$ pF)	0.5 fC (0.13 MIP)
Output voltage swing	5.6 V
Maximum allowed input current	400 nA/channel
Peaking time	250 ns
Linearity	1% (full range)
Resolution	± 1 MIP
Gain spread	$\pm 1\%$
Cross talk (depends upon HOLD timing)	-1.6 to -2.2%
Command signals (ECL)	CLOCK, PRESET, CHANNEL SELECT
Fast-OR linearity range	500 MIP
Internal calibration capacitors	2 pF ($\pm 0.3\%$ within chip)
Power consumption	200 mW/chip

Table 2:   Specifications of the AMPLEX-SICAL multiplexed charge amplifier.

Trigger	Description	Threshold(s)	Down scale factor	Rate $\mathcal{L} = 10^{31}$
$(A_{high} \cdot B_{low})$ $(A_{low} \cdot B_{high})$	Double-arm (Bhabha coincidence)	$\geq 24GeV$ $(high)$ $\geq 12GeV$ (low)	1	2 Hz
$A_{very\ high}$ $B_{very\ high}$	Very high single-arm (trigger efficiency)	$\geq 39GeV$ $(very\ high)$	2	1 Hz
$A_{very\ low}$ $B_{very\ low}$	Very low single-arm (beam background)	$\geq 9GeV$ $(very\ low)$	2500	50 mHz

Table 3: Luminosity triggers. Inclusive rates (downscaled) are given for a typical LEP luminosity of $10^{31}cm^{-2}s^{-1}$. Typical very high single-arm exclusive rate is 120 mHz.
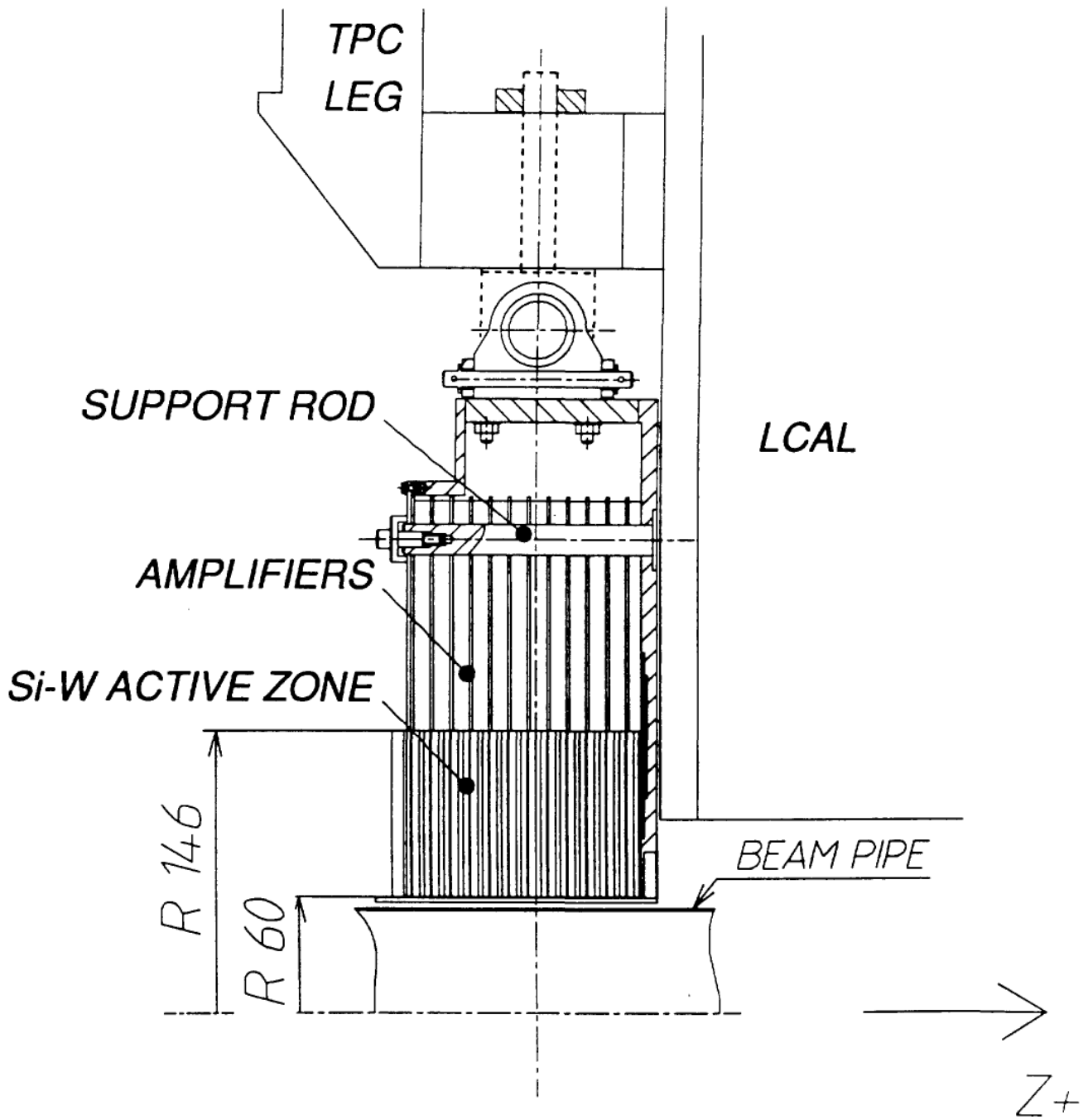
Figure 1: Section view of one SICAL calorimeter. The twelve sampling layers are formed from W-Si-W minimodules which are supported internally on rods passing through G-10 and aluminium support plates.
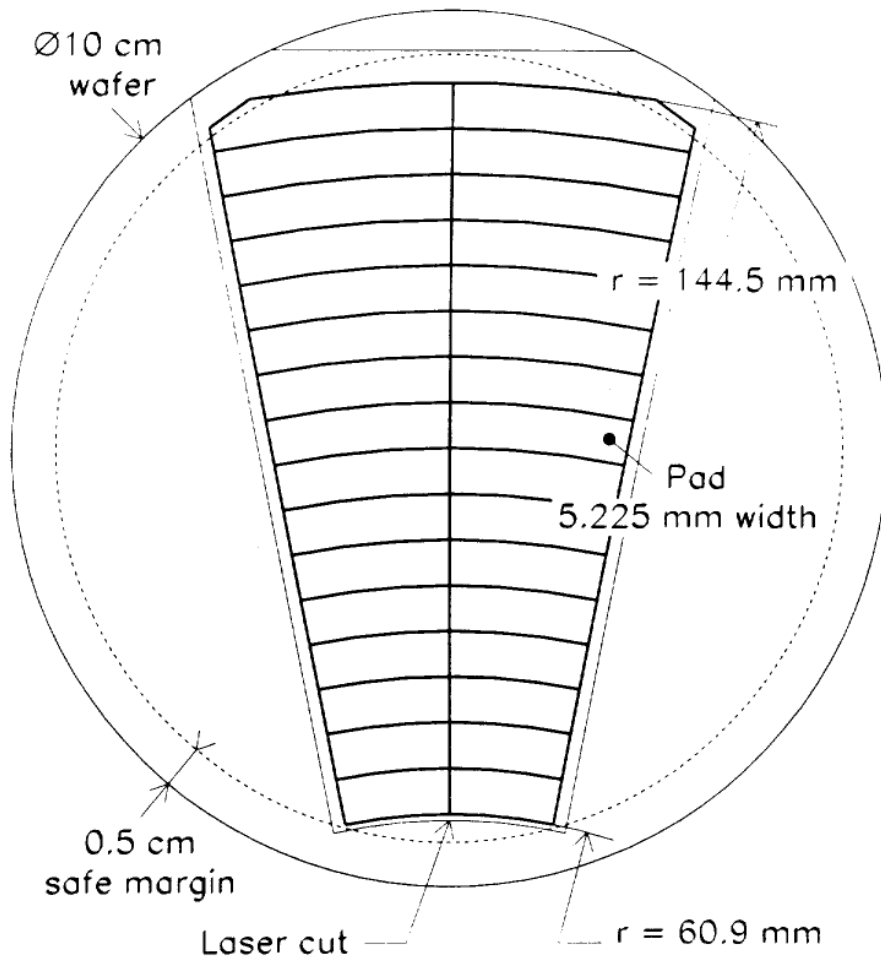
Figure 2: Silicon detector. Sectors ($2 \times 11.25°$) are cut from $300\mu m$ thick, 10 cm diameter, high resistivity wafers. The rounded lower radial edge is laser cut. Radial padwidth is $5.225mm$.
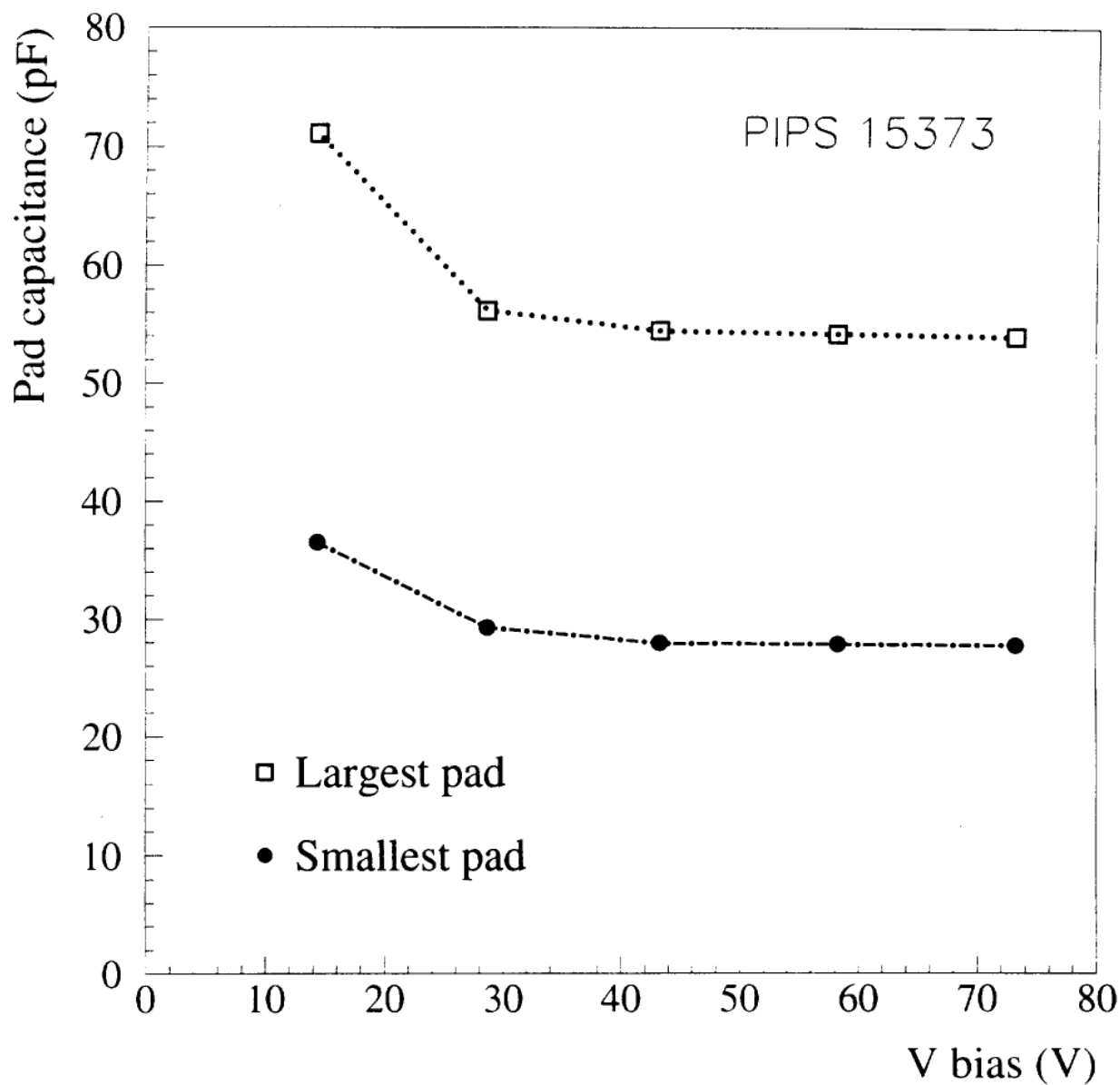
Figure 3: Depletion curves for the largest (open squares) and smallest pads (full circles) of a typical silicon detector, showing full depletion at 35 V.
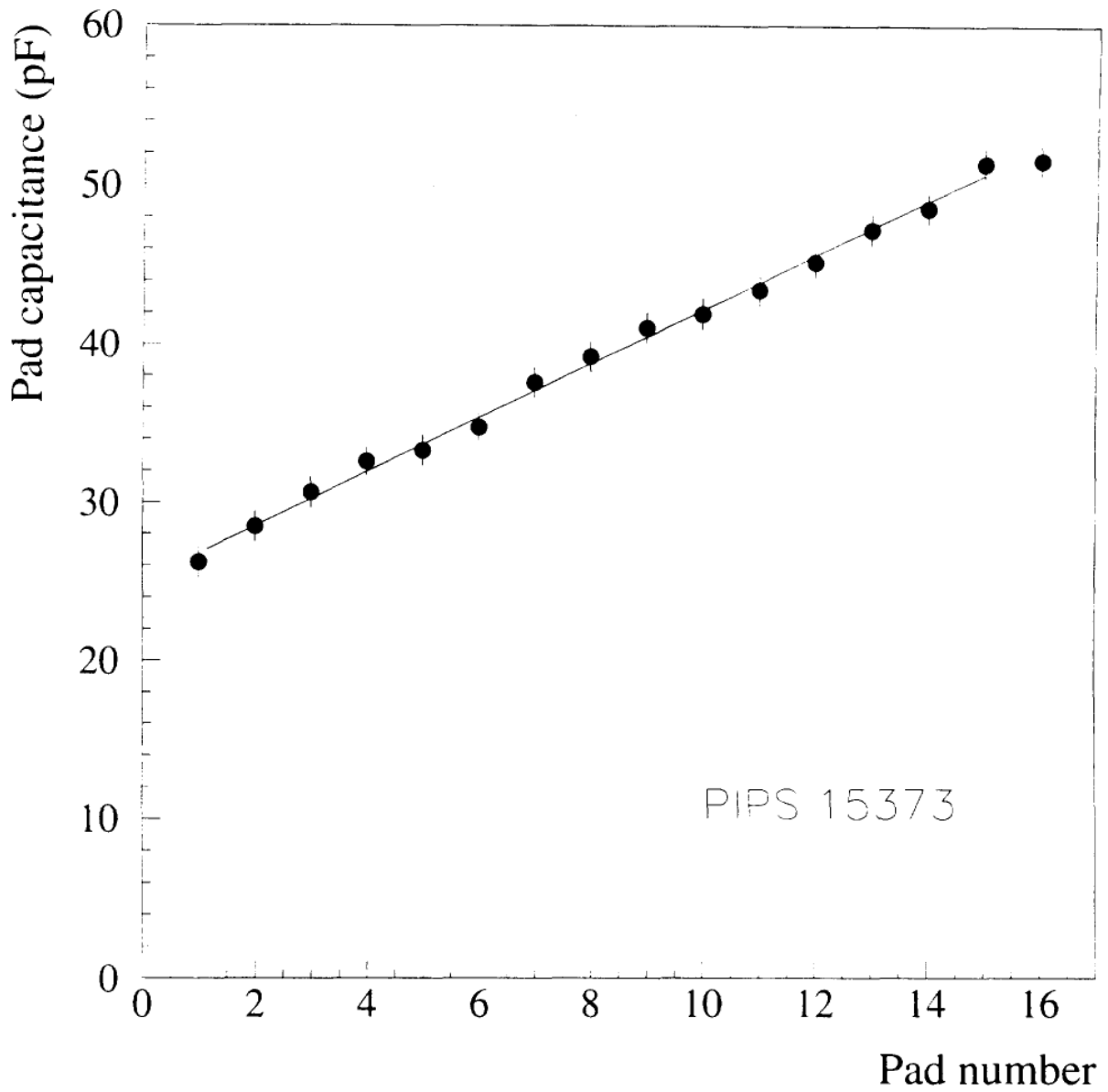
Figure 4: Silicon detector capacitance of a fully depleted crystal varies linearly from 25 pF (inner radius) to 50 pF (outer radius).
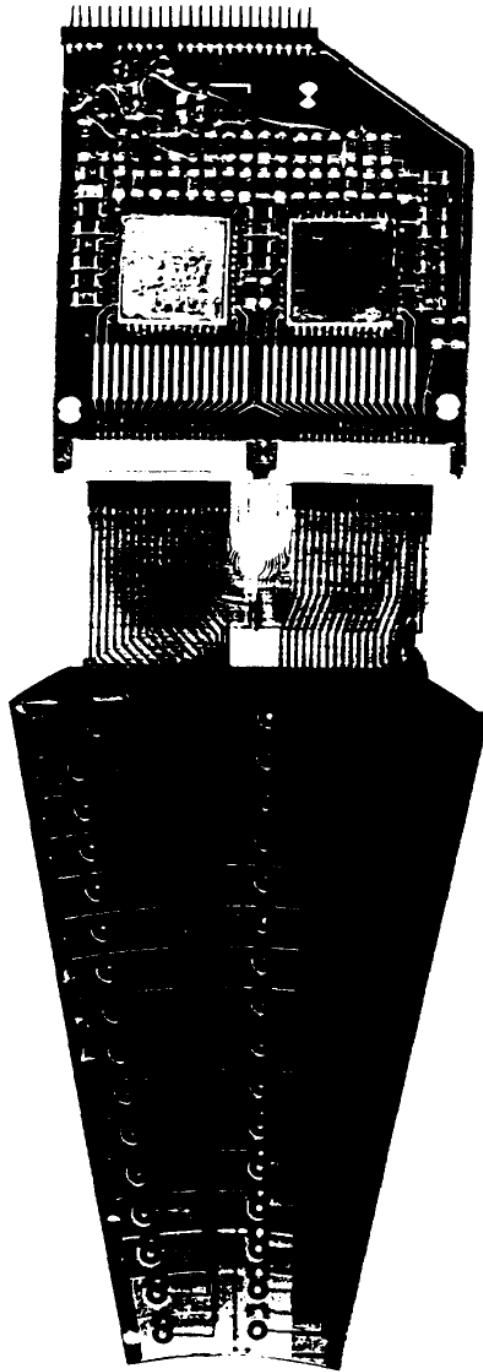
Figure 5: Silicon detector mounted on its ceramic support (CESIKA assembly). Two charge amplifiers each serve 16 radial pad rows in a single 11.25° azimuthal slice. Connection to the pads is obtained via printed kapton foil.
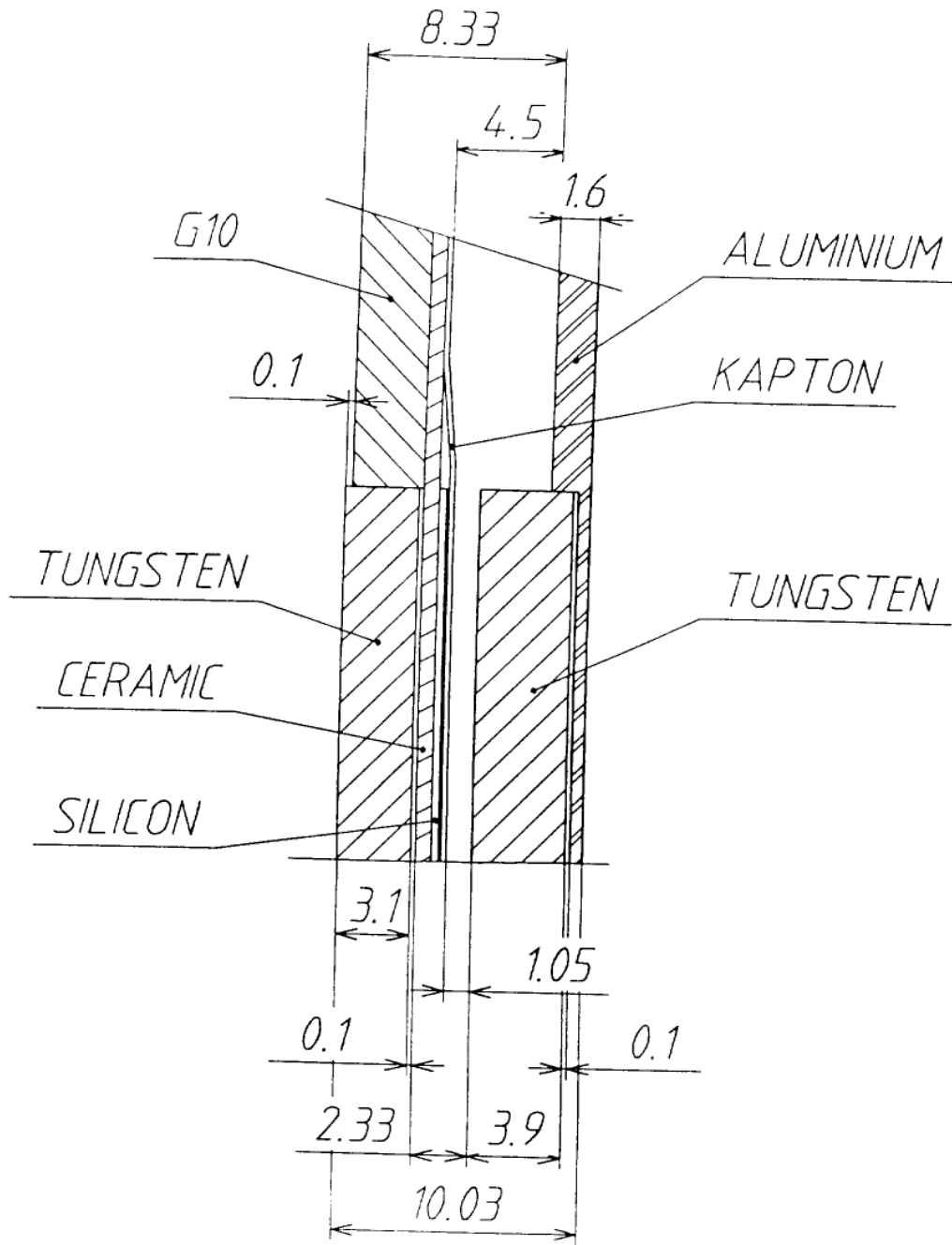
Figure 6: Detail section view of a minimodule composed of two W plates sandwiching a "G-10" layer which supports the silicon detectors (dimensions in mm).
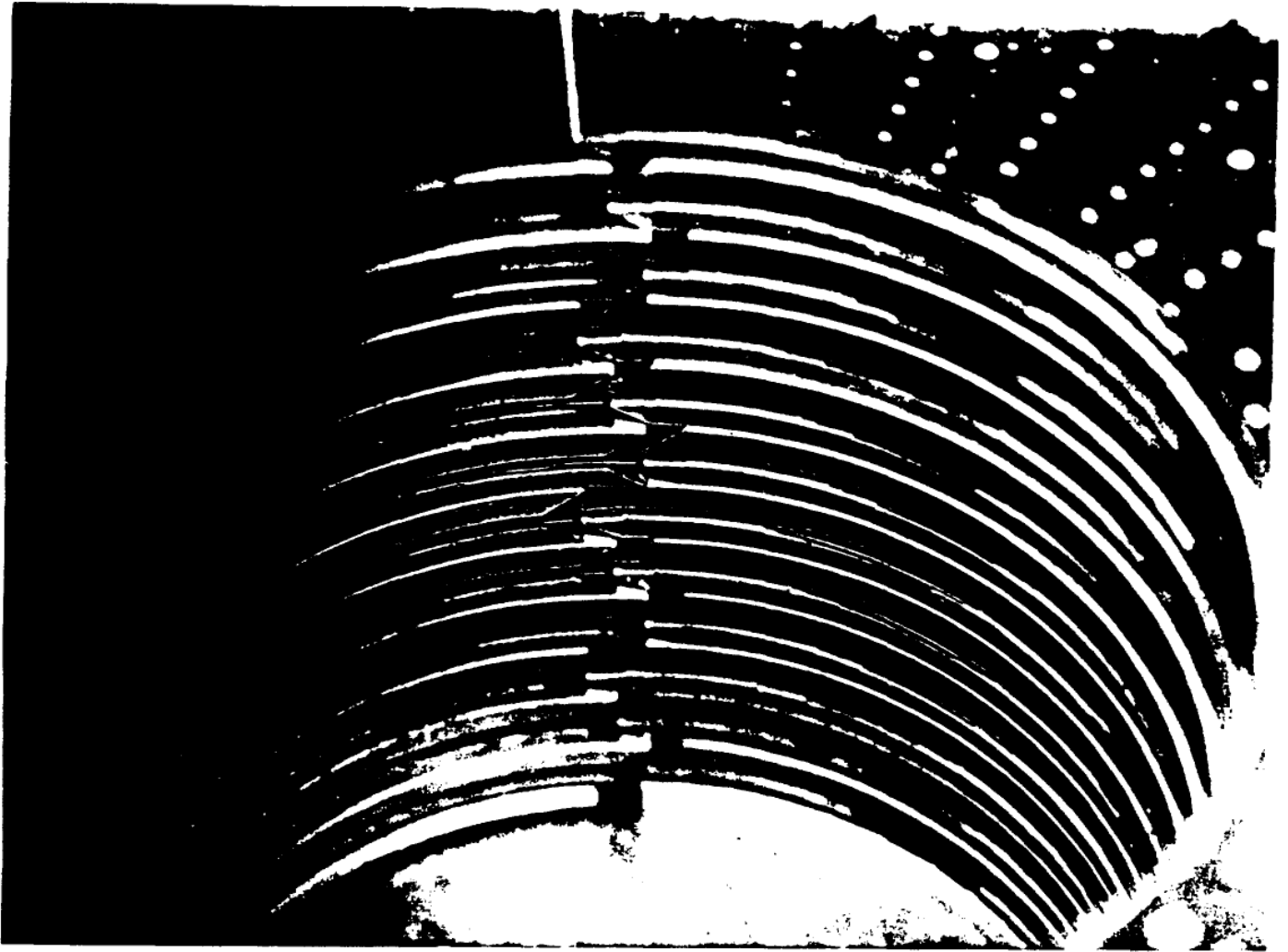
Figure 7: Detail photograph of the staggered crack between two half-calorimeters, taken during an assembly test prior to detector completion. The angled cut of the tungsten plates is clearly visible.
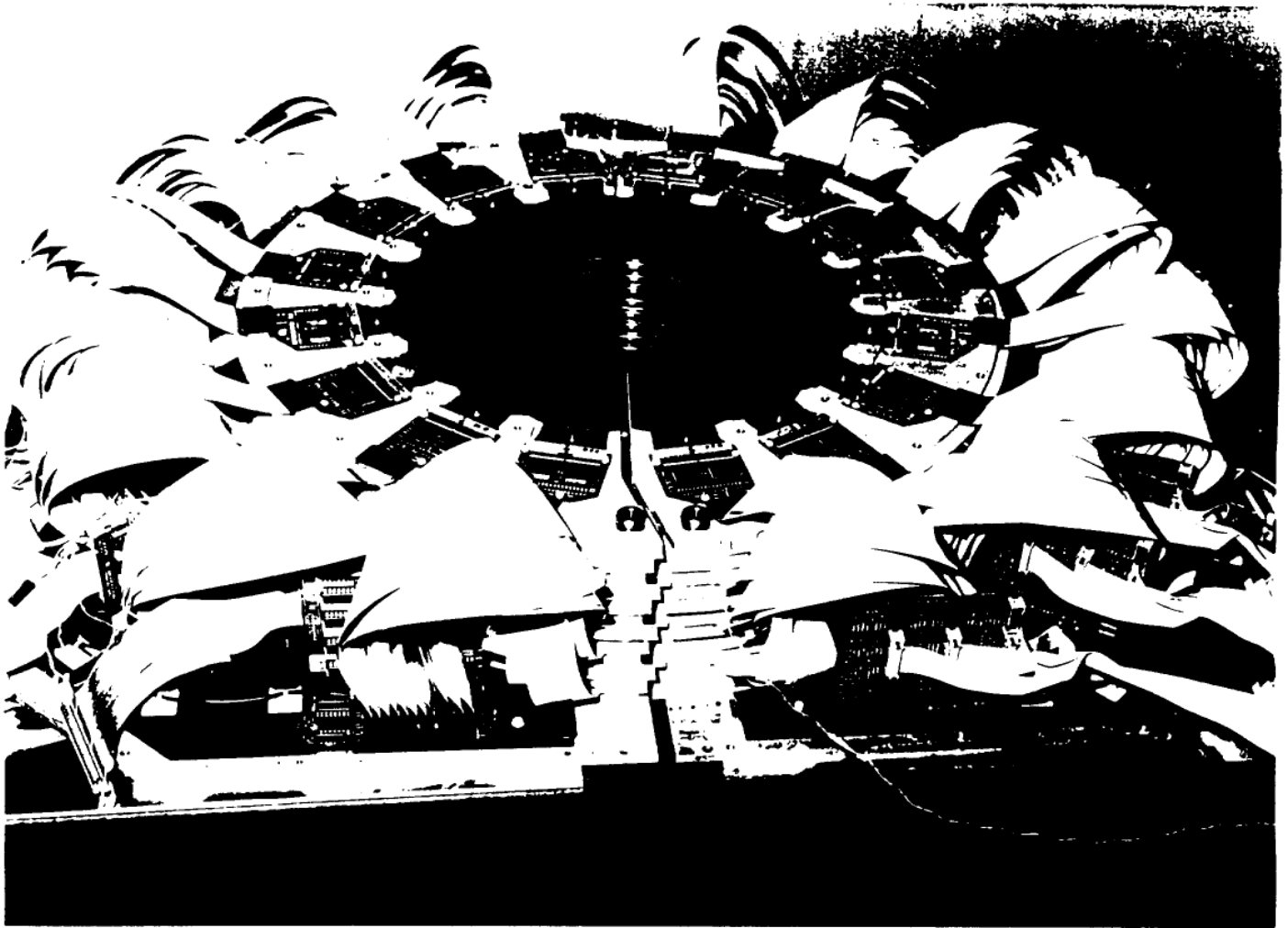
Figure 8: Stacking of calorimeter minimodules. The support rods position each minimodule to a precision of $10\mu m$. The staggering of the successive minimodules to avoid aligned cracks can be seen in this photograph.

Figure 9: AMPLEX-SICAL schematic diagram.
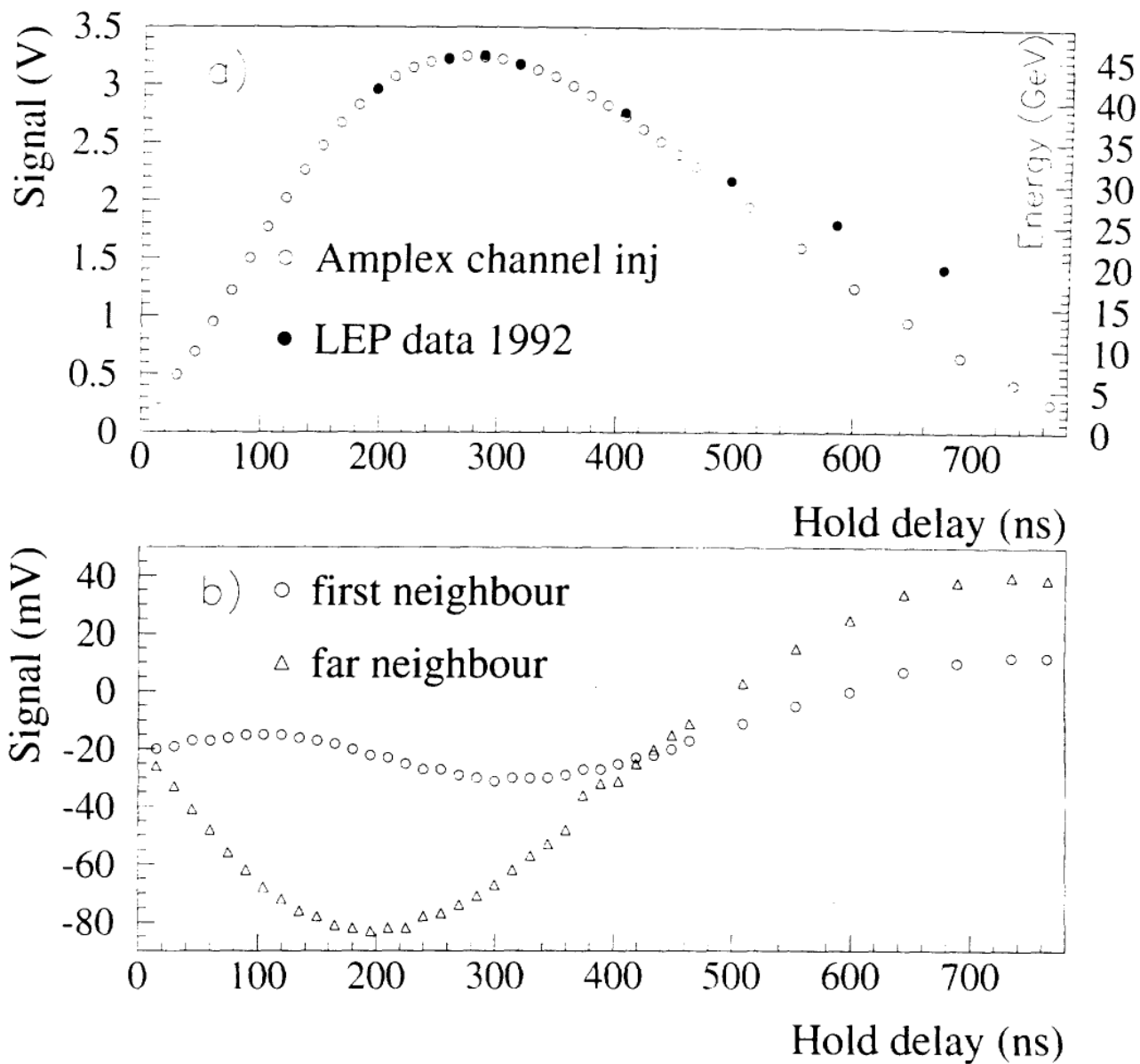
Figure 10: (a) Single channel output (V) versus HOLD delay. Cross-talk effects are seen when summing over showers (LEP data in full circles) taken at different HOLD settings. (b) Cross-talk on the same chip (note scale in mV) connected to a silicon detector. Adjacent pad coupling (open circles) differs from the chip substrate effects seen in a more distant pad (triangles).
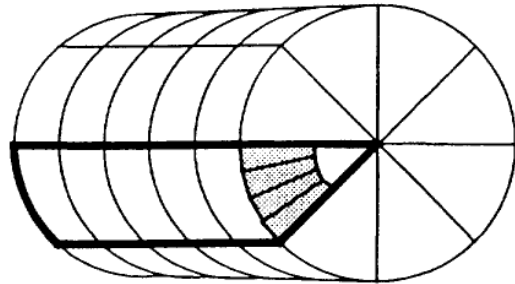
"Road 1"
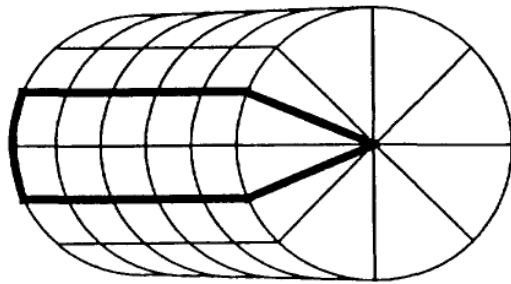
"Road 2"

Figure 11: Trigger segmentation: each trigger sector is 45° wide. Two sub-divisions, "Road 1" and "Road 2", offset with respect to each other by 22.5° (2 AMPLEX), ensure that a shower is fully contained in at least one.

30
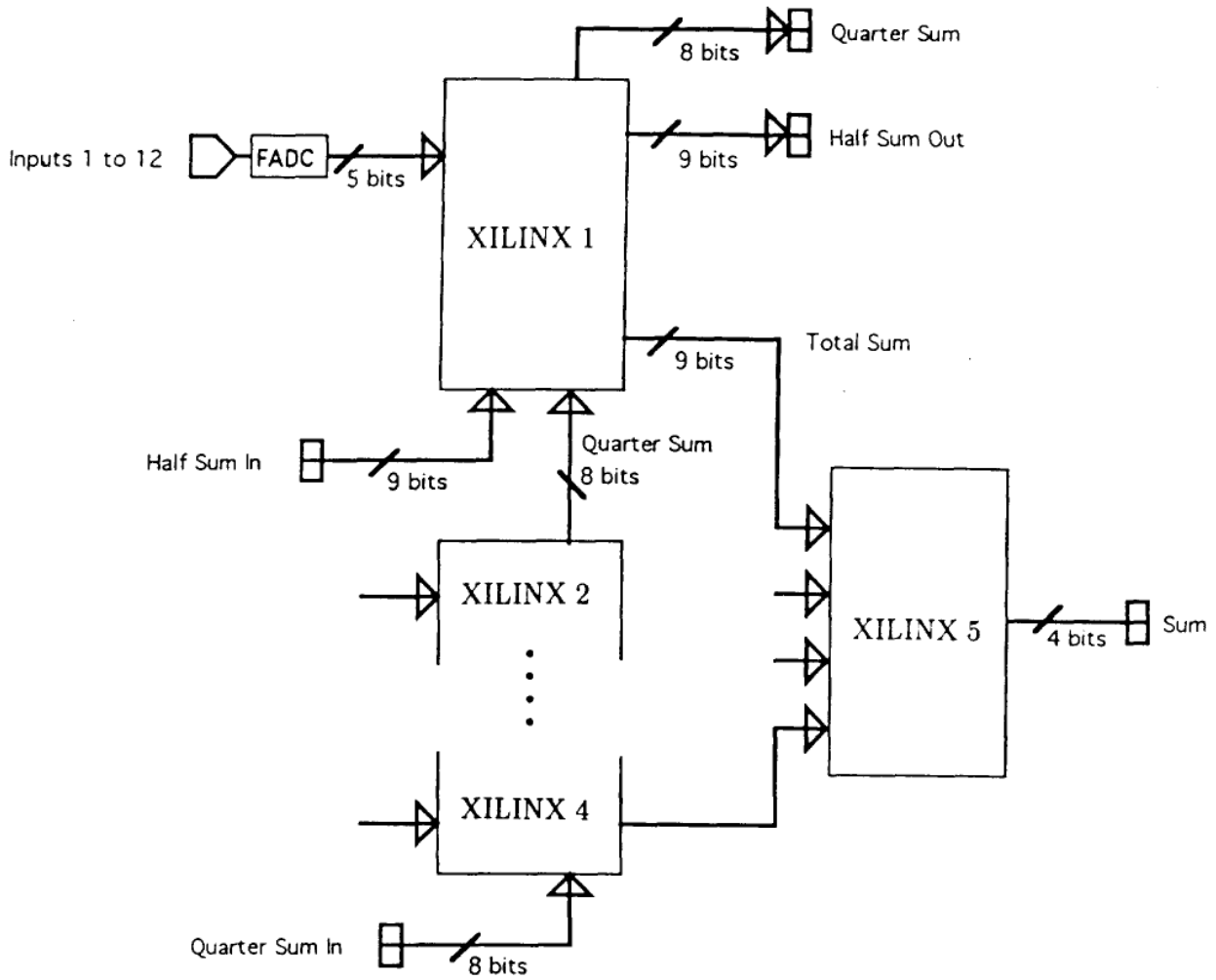
Figure 12: Trigger mixer card block diagram. Four XILINX programmable gate arrays are used as adders to build the trigger digital partial sums, and the fifth XILINX is used as a comparator to construct the trigger masks.
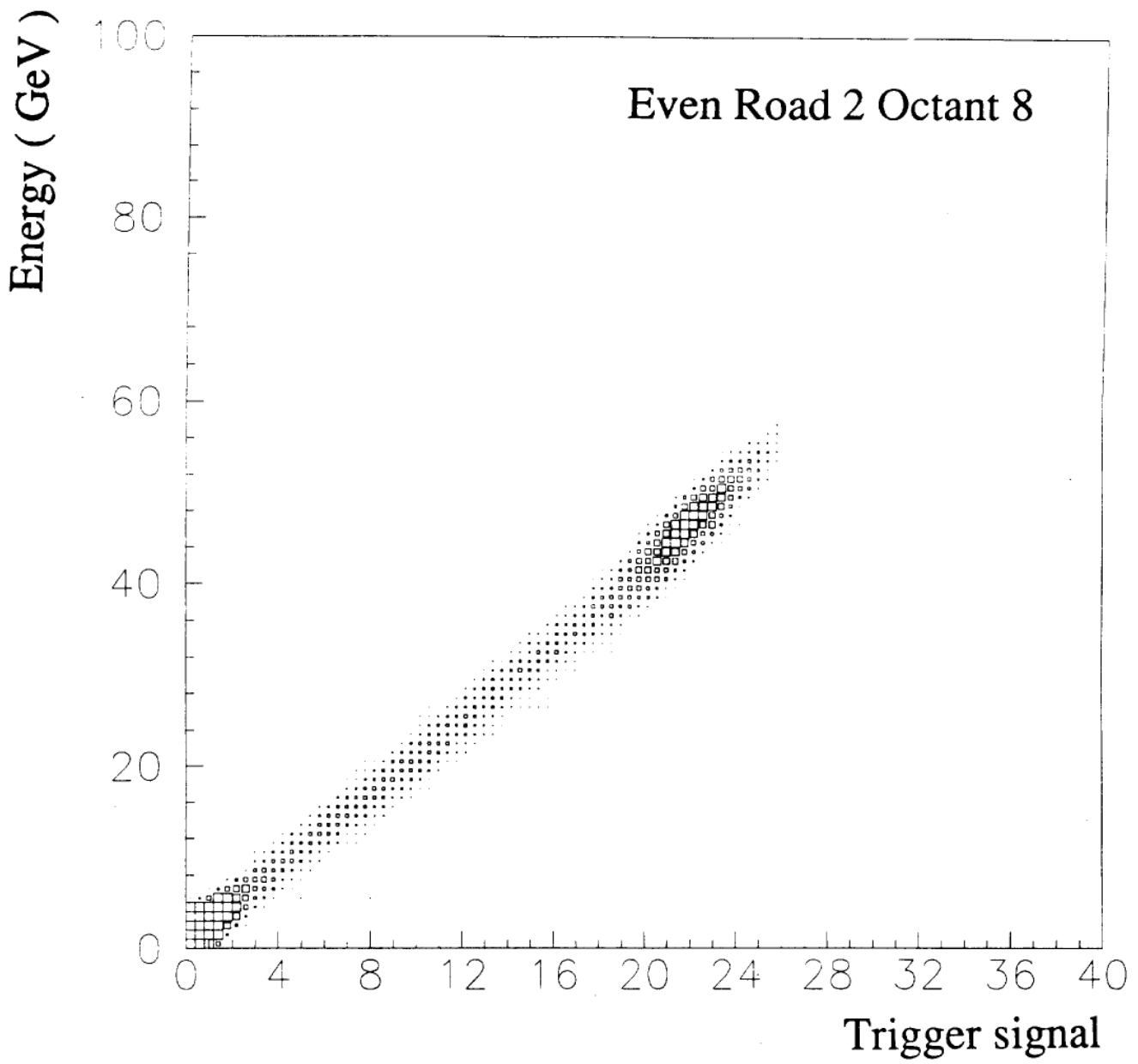
Figure 13: Trigger signal versus read-out energy for a typical trigger sector. Sectors contain only odd or even planes. so the Bhabha events form a peak at half the beam energy.
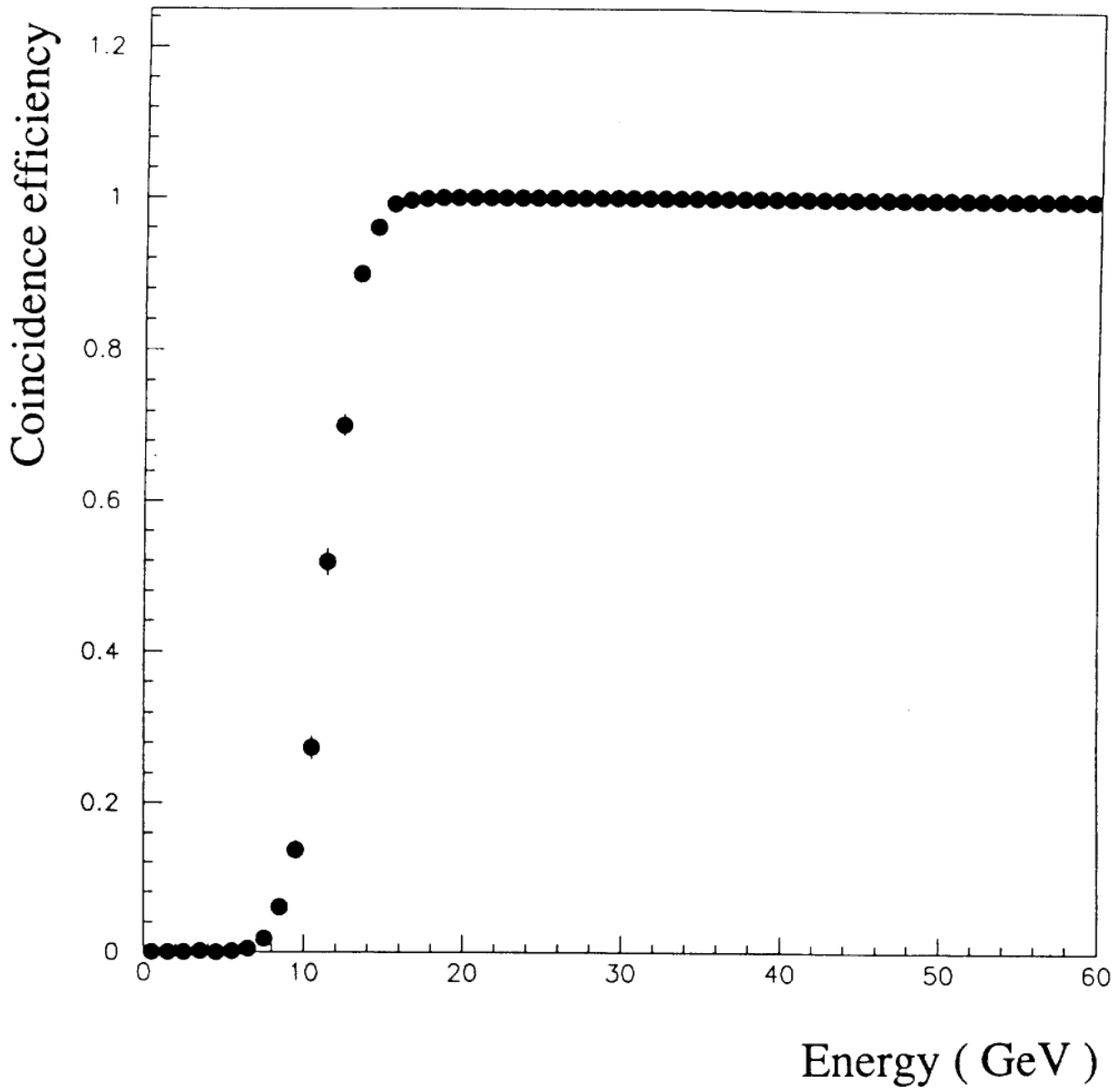
Figure 11: Efficiency of the the coincidence trigger versus energy on the low side. The very high threshold single-arm trigger is used to measure this efficiency.
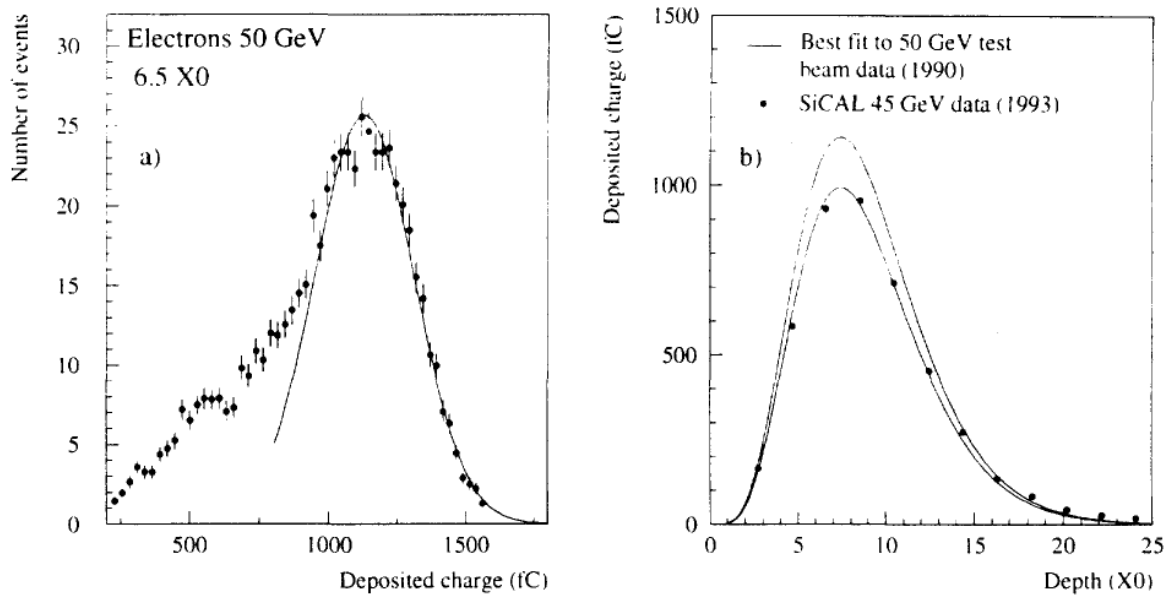
Figure 15: Charge (fC) deposited in a single pad (shower centered) versus shower depth: (a) distribution of deposited charge at $6.5.X_0$, Gaussian fit gives most probable value: (b) Most probable value versus depth, smooth curve (without points) is a fit to 50 GeV e^- test beam prototype measurements. Points are 45 GeV Bhabha events taken at LEP.
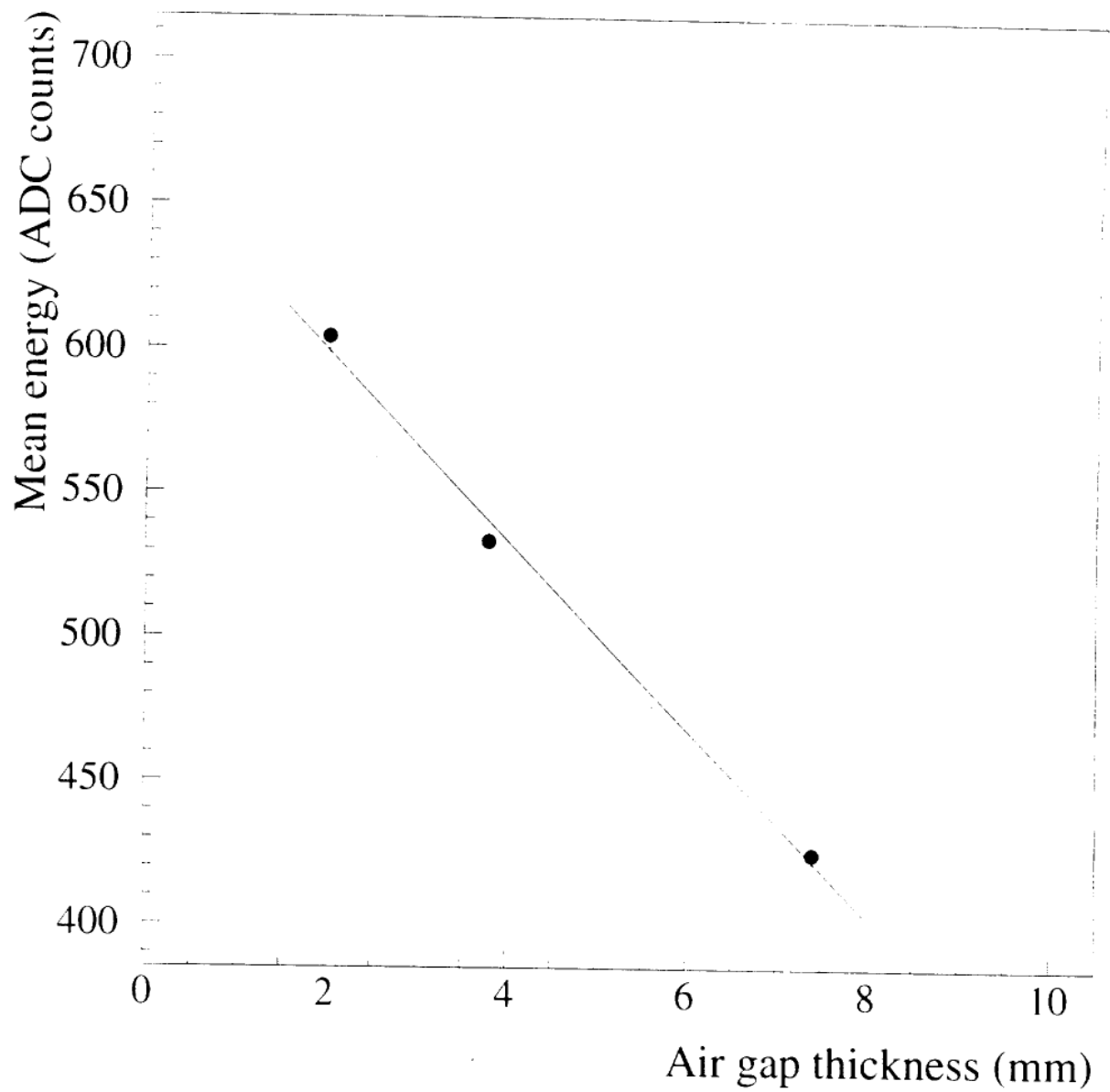
Figure 16: Prototype test of single layer response versus air gap between the silicon and tungsten.
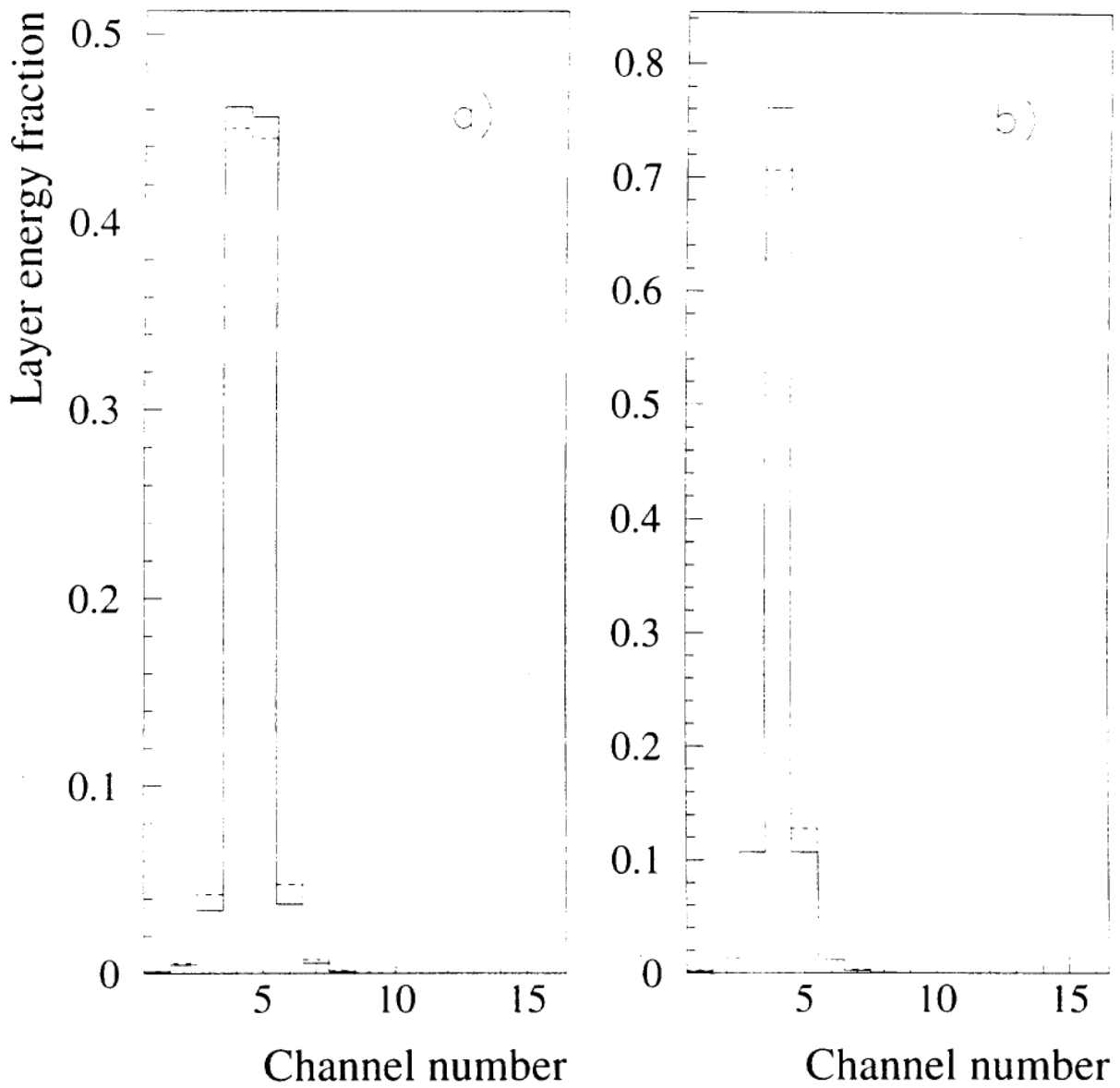
Figure 17: The radial energy distribution at $6X_0$ (solid line) and $8X_0$ (dashed line) over a single ϕ-padwidth for 45 GeV showers (LEP data): (a) showers centered between pads 4 and 5, and (b) centered on pad 4.
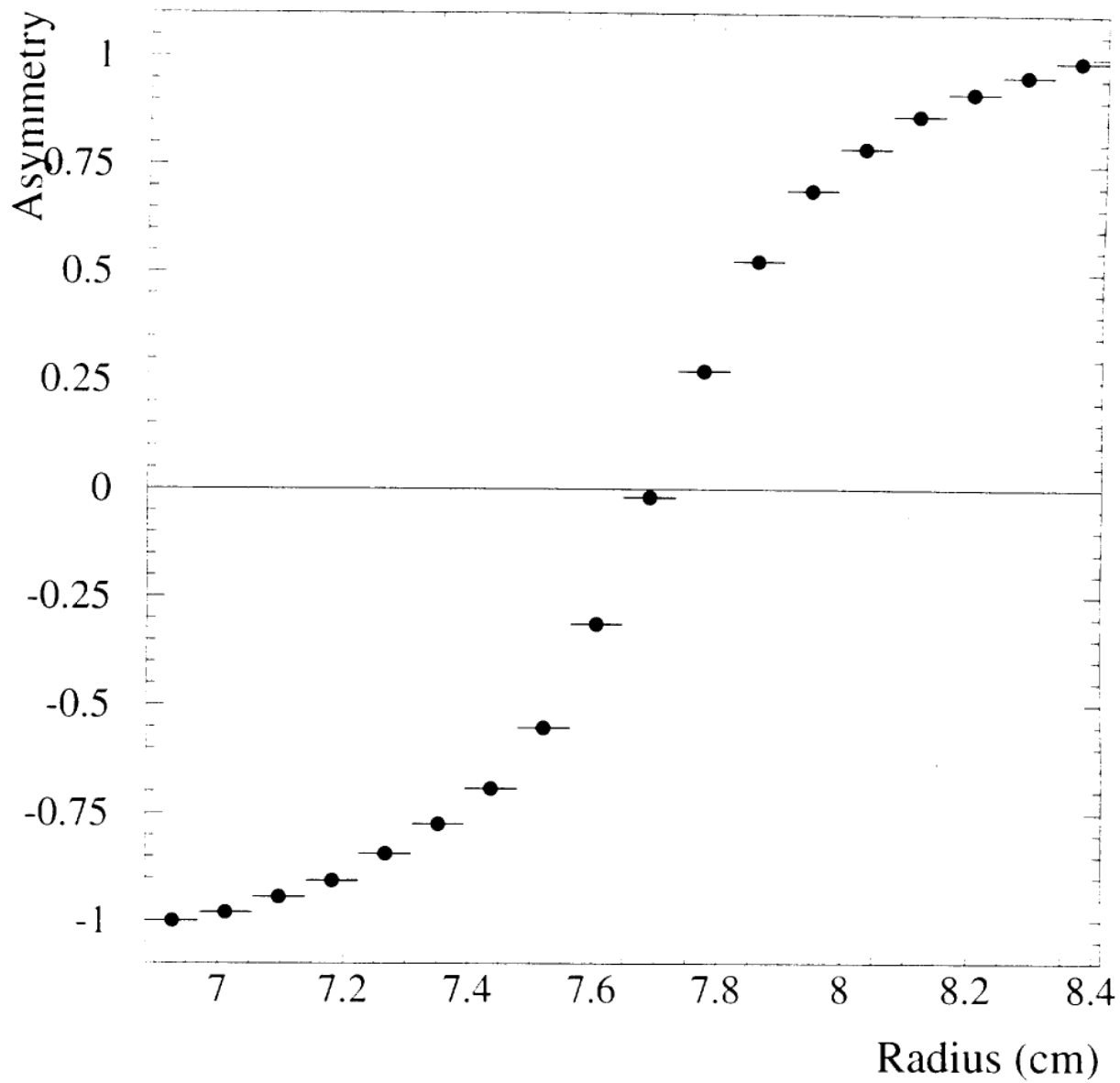
Figure 18: The radial energy asymmetry, A_r shown versus the cluster radial position near the pad 3-4 boundary.
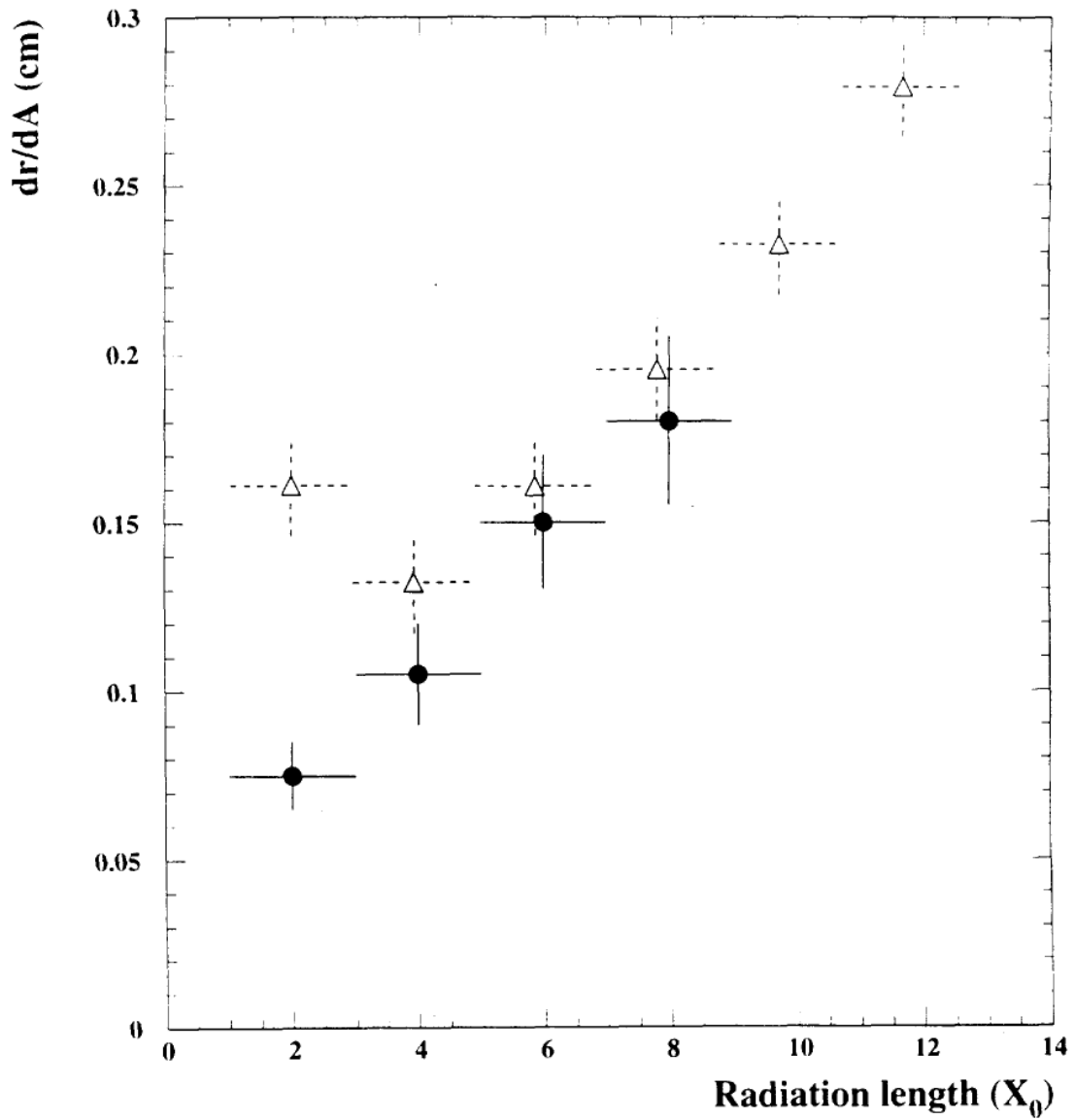
Figure 19: Slope of the energy sharing asymmetry $(dA_r/dr)^{-1}$ at the boundary (pads 4 and 5) versus shower depth (X_0). Prototype (final design) values shown as solid points. LEP data shown as open triangles.
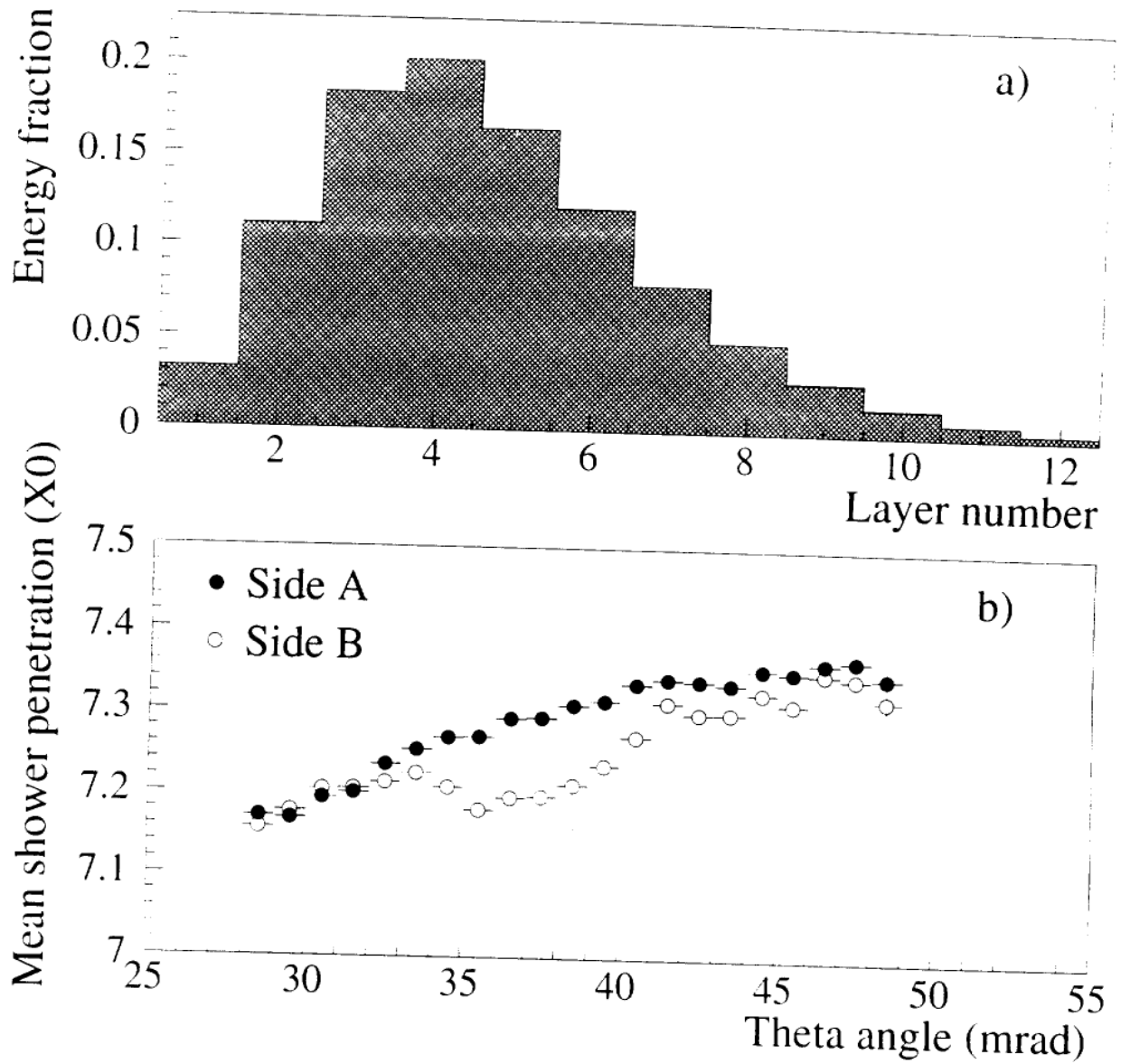
Figure 20: (a) Longitudinal shower profile for Bhabha events (1.91 X_0/layer). (b) The relative mean shower depth for Bhabha events versus polar angle for side A (solid points) and side B (open circles). Structure on B-side (31 to 41 mrad) is a support ring removed on side A.
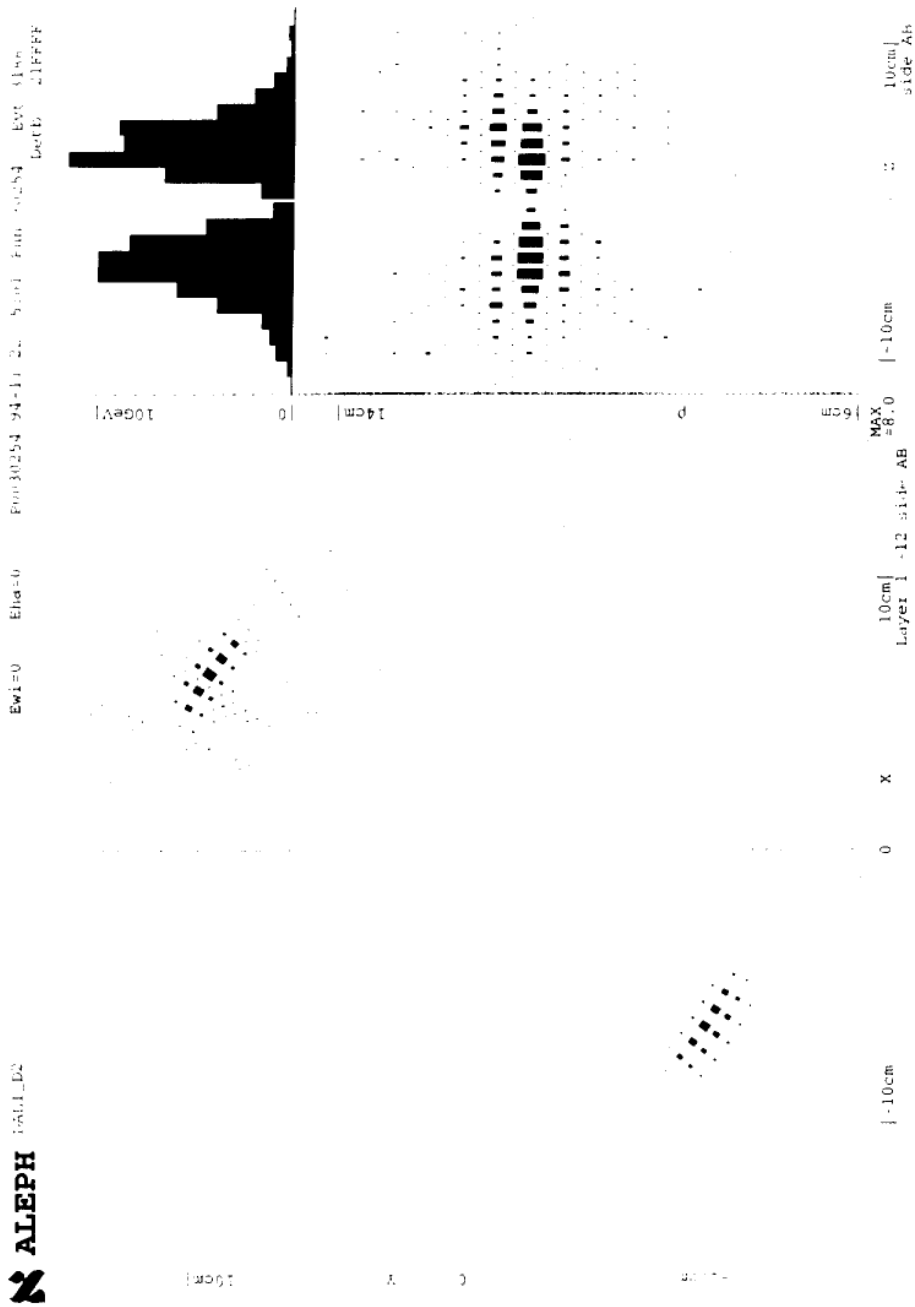
Figure 21: Typical Bhabha event display (DALI). Clusters on A and B side are shown in the same view. z-profiles are shown from the IP toward +z or -z; they are the sums of pad energies over R-ϕ for each side.
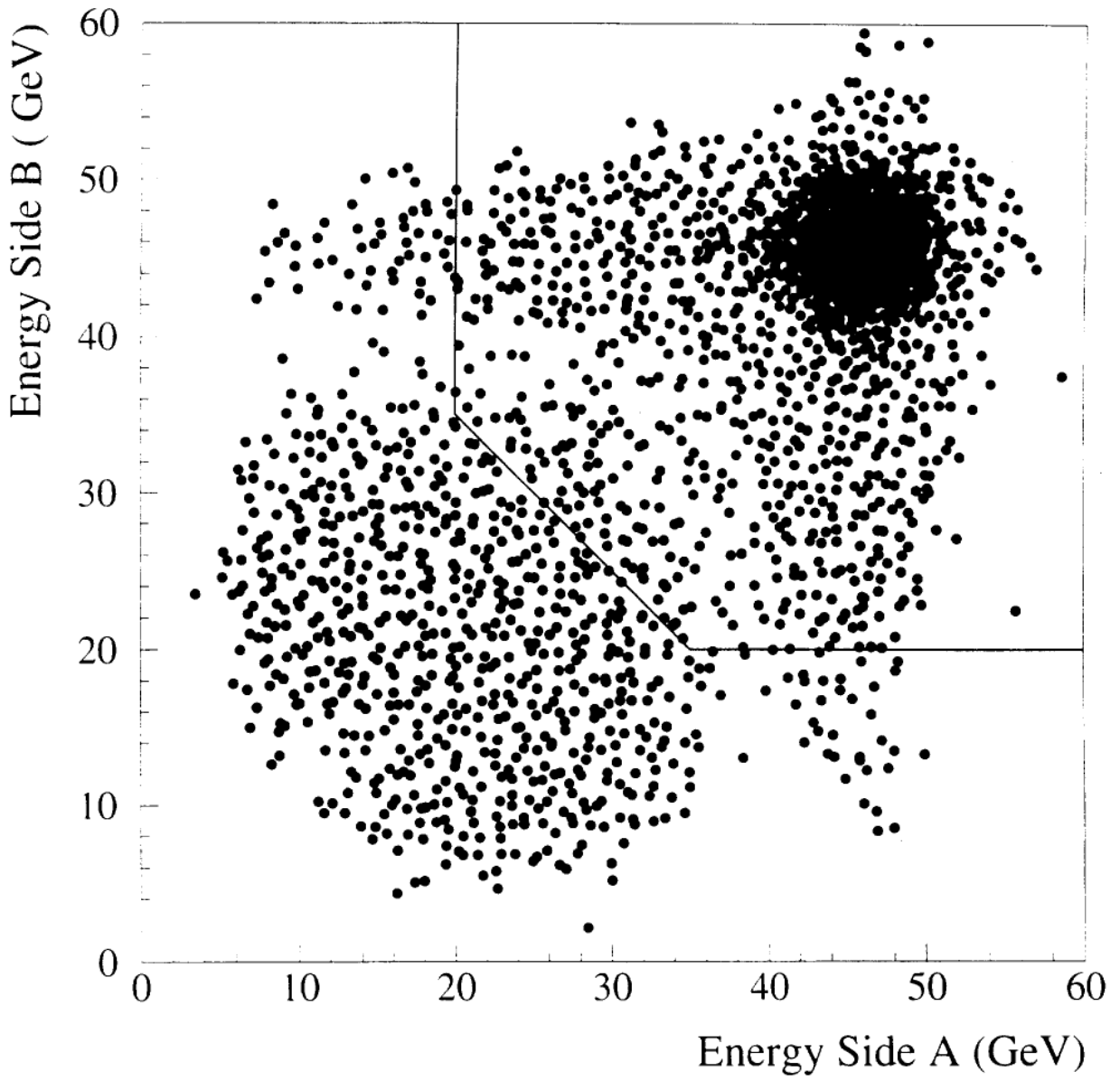
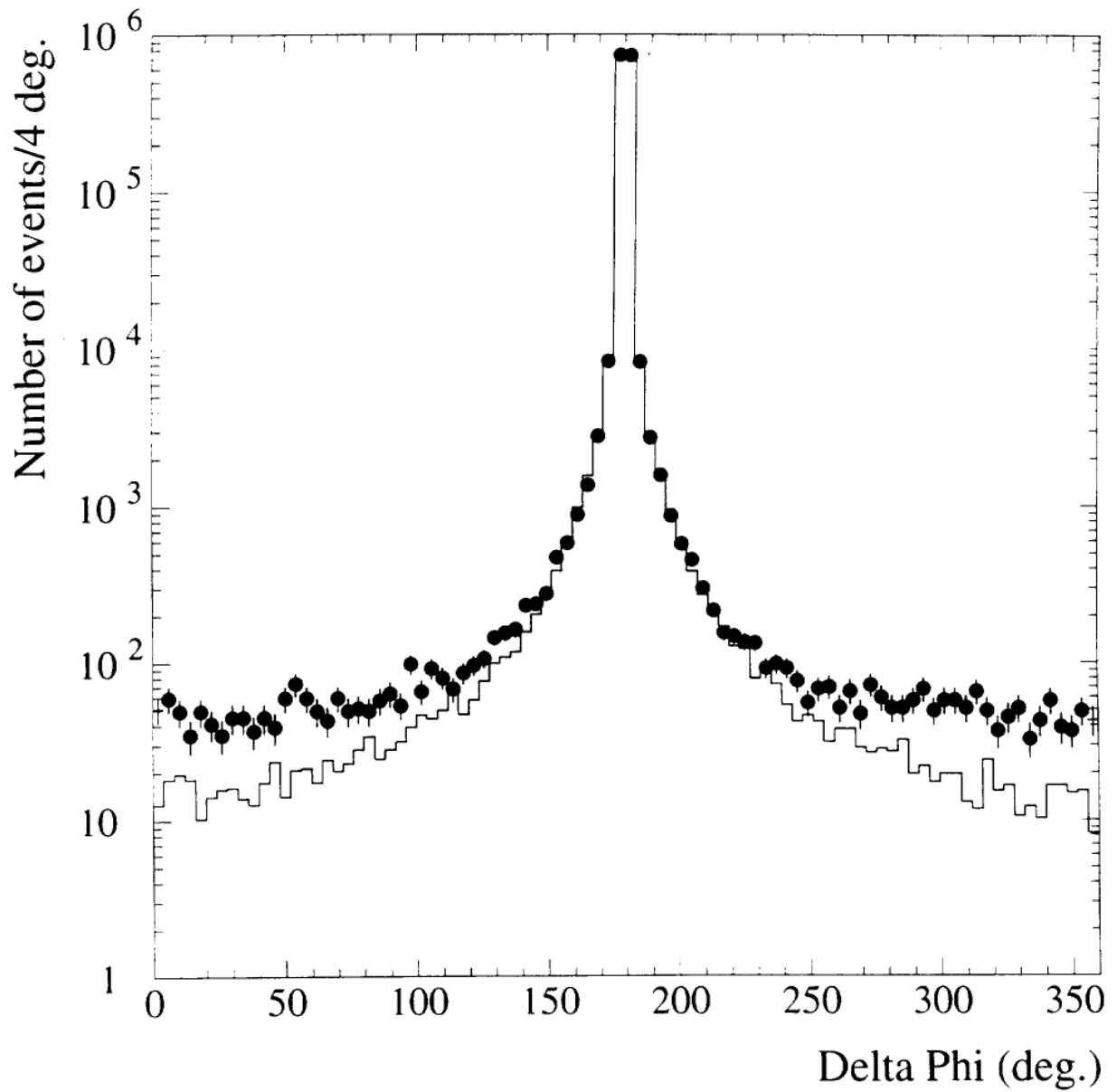Figure 22: Largest reconstructed cluster energy on Side-A versus largest reconstructed cluster energy on Side-B (GeV).

Figure 23: Distribution of the φ-difference Δφ between the "tight-side" and "loose-side" clusters. Data are plotted as points and the Monte Carlo (without background) is shown as a line.
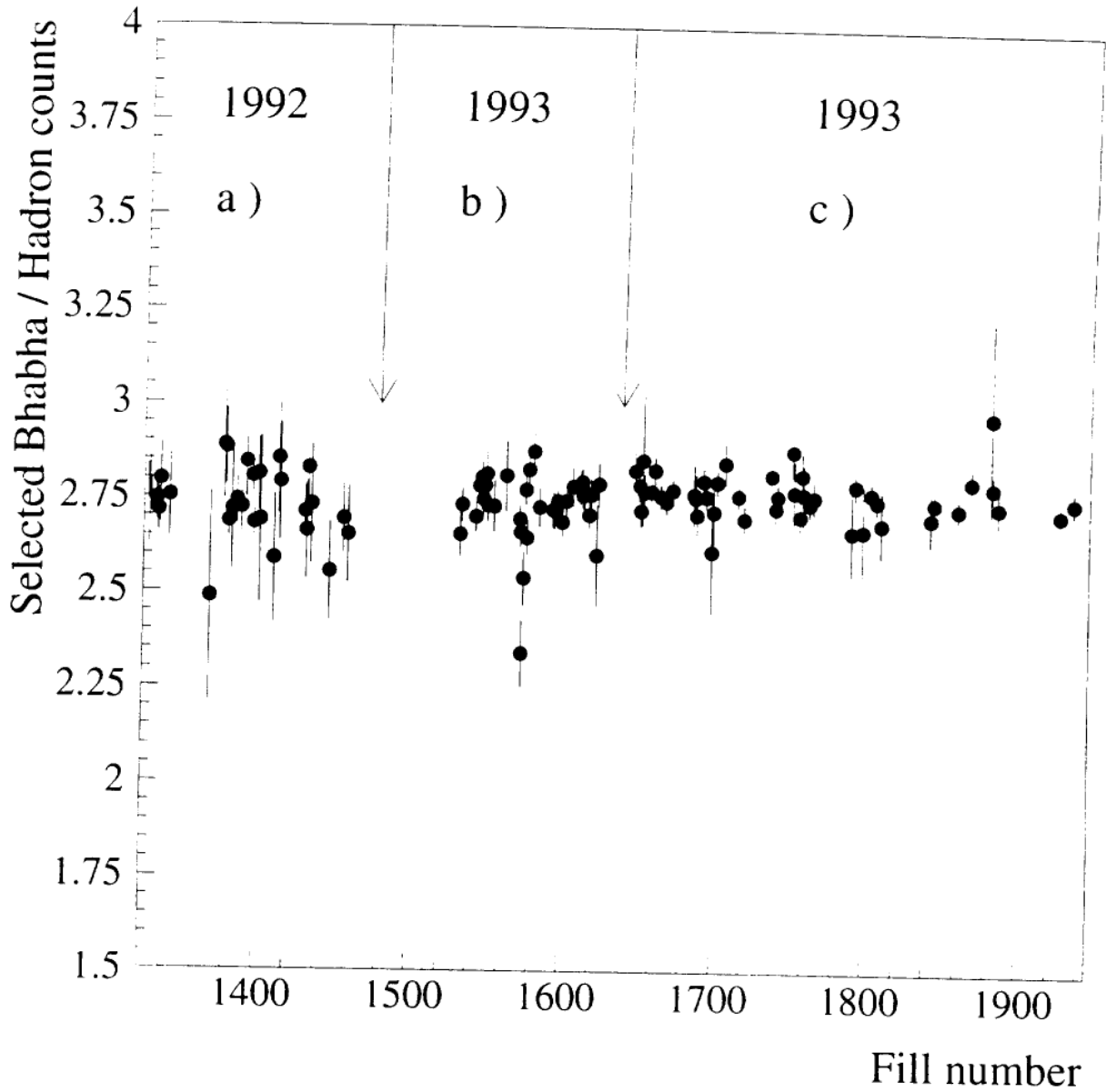
Figure 24: Ratio of background corrected Bhabhas to hadronic events taken at the Z peak (TPC and calorimeter selections averaged), plotted versus fill number: (a) two months at the end of 1992, (b) one month pre-scan period of 1993, and (c) 5 month Z resonance scanning period of 1993.

43